

## Elastic scattering of 80–180 MeV protons and the proton-nucleus optical potential

A. Nadasen,\* P. Schwandt, P. P. Singh, W. W. Jacobs, A. D. Bacher, P. T. Debevec,† M. D. Kaitchuck, and J. T. Meek

*Indiana University Cyclotron Facility, Bloomington, Indiana 47405*

(Received 11 August 1980)

Accurate and extensive measurements have been made of the differential cross sections for the elastic scattering of protons from  $^{40}\text{Ca}$ ,  $^{90}\text{Zr}$ , and  $^{208}\text{Pb}$  targets over an energy range of 80–180 MeV, in the angular range from about  $6^\circ$  to about  $90^\circ$  (to  $126^\circ$  for  $^{90}\text{Zr}$  at 135 MeV) in  $0.5^\circ$  to  $2.5^\circ$  steps. The most prominent general feature of the data, namely strong damping of the diffractive oscillations in the mid-angle region (roughly  $30^\circ$ – $60^\circ$ ), was found to arise from the complex spin-orbit interaction which has a considerably greater influence on the differential cross section at these energies than at lower energies. These data, together with data of comparable quality from other sources in the energy range 60–180 MeV, were analyzed in terms of a 10-parameter phenomenological optical-model potential using relativistic kinematics and a relativistic extension of the Schrödinger equation. Analyses with various parameter constraints were performed. A logarithmic energy dependence was found for the strengths of the real potentials (central and spin-orbit terms); the corresponding imaginary potentials were found to be essentially independent of energy. While individual model parameters were generally not uniquely defined by the cross section data, volume integrals of the central potentials were well determined. The spin-orbit parametrization was found to be relatively more uncertain, despite the enhanced sensitivity of the cross section to spin dependent terms in the potential at these energies and the inclusion of some existing polarization data in the analysis. Some features of the phenomenological potentials were compared with the predictions of microscopic potential models, and certain aspects of the proton-nucleus interaction at the higher energies have been found to be describable in terms of the free nucleon-nucleon interaction.

NUCLEAR REACTIONS  $^{208}\text{Pb}(p,p)$ ,  $E_p = 79.9, 121.2, 160.0, 182.4$  MeV;  $^{90}\text{Zr}(p,p)$ ,  $E_p = 79.8, 135.1, 160.0, 180.0$  MeV;  $^{40}\text{Ca}(p,p)$ ,  $E_p = 80.2, 135.1, 160.0$  MeV; measured  $\sigma(\theta)$ ; optical-model analysis, deduced energy and target mass dependences of the potential; compared phenomenological results to those of microscopic models.

### I. INTRODUCTION

Extensive and precise measurements of observables (differential cross sections and polarizations) for the elastic scattering of protons from nuclei over broad ranges of proton energy and target mass are important from two general viewpoints, both of which have guided the thrust of the present study. First, such data are important for generating a systematic, global, phenomenological optical-model description of the nucleon-nucleus interaction. Such an empirical parametrization of the scattering is useful as input for distorted-wave Born approximation (DWBA) or impulse approximation (DWIA) calculations of inelastic scattering or reactions, as well as for coupled-channels descriptions. Beyond this utilitarian aspect of the optical model, it is of fundamental interest to determine the systematic dependence on energy and target mass of quantities which are relatively free from ambiguities in parametrization, such as the volume integrals of the various nuclear potentials and their root-mean-square radii. Second, such measurements are an important ingredient for understanding the nucleon-nucleus interaction on a microscopic level, starting from the free nucleon-nucleon in-

teraction and incorporating various many-body effects pertinent to nucleon propagation in nuclear matter in general and in finite nuclei in particular. The developments in this regard have primarily been directed towards constructing the generalized optical potential and (1) comparing it (in a local approximation) with phenomenological potentials, and (2) calculating observables for direct comparison with experimental data.

Extensive studies of proton elastic scattering from a large sample of nuclei have been reported for bombarding energies up to about 60 MeV. Examples in the 10–20 MeV proton energy range can be found in Refs. 1 and 2, at 30 MeV in Refs. 3 and 4, at 40 MeV in Refs. 5 and 6, and at 61 MeV in Ref. 7. Measurements at proton energies of 100 MeV,<sup>8</sup> 156 MeV,<sup>9</sup> 156 MeV,<sup>10</sup> 185 MeV,<sup>11,12</sup> and more recently at 613 MeV,<sup>13</sup> 800 MeV,<sup>14</sup> and 1040 MeV<sup>15</sup> are also available. From this data base, with relatively few measurements at the higher energies, a number of curious, and in some cases apparently inconsistent, features arose from analyses of the data in terms of a local optical potential model. For example, it became apparent that, whereas below 60 MeV the volume integral  $J_R$  of the real central potential decreased linearly with energy at the rate of about  $2.0 \text{ MeV fm}^3/\text{MeV}$ ,<sup>7</sup> a logarithmic dependence of the form  $J_R(E_p) = J_R(0)$

$-\beta \log E_p$  (Ref. 11) was more consistent with the available results over the broader energy range of 40–1000 MeV. Alternatively, when the values of  $J_R$  were displayed<sup>16</sup> as a function of the relativistic kinematic factor  $1/\gamma$ , where  $\gamma = (1 + E_p/mc^2)$ , they were found to decrease linearly up to 150 MeV and also linearly from 150 to 1000 MeV but with a different slope for the two energy regions. This seemingly erratic behavior of  $J_R$  is unexpected and not readily understood. A precise determination of the energy dependence of  $J_R$  over a wide energy range is important in order to elicit the extent to which the observed  $E_p$  dependence of the local potential is a trivial one (arising from the nonlocal nature of the proton-nucleus interaction) or is dynamic (has its origin in the intrinsic energy dependence of the two-nucleon force). Optical-model analyses of the available data further revealed that the root-mean-square radius of the real central potential was largely independent of proton energy up to 60 MeV and also between 155 and 185 MeV, but was systematically larger by roughly 30% at the lower energies. This behavior of the rms radius, if real, may be reflecting the appreciable Pauli blocking effects expected at low energies (i.e., reduction of the interaction strength in the high-density nuclear interior) and a decrease in the range of the fundamental nuclear force with increasing energy.

The above observed characteristics of the phenomenological parameters may thus be closely tied to the more fundamental aspects of the optical potential and can be expected to provide specific tests of the validity of various microscopic formulations of the optical model. However, some of the general features of the phenomenological model inferred from previously existing data above 60 MeV may well be misleading in view of (a) the paucity of data above 60 MeV, (b) the restricted angular range of the data at energies above 150 MeV, (c) the different methodologies used in the analyses (such as treatment of relativistic effects which become progressively more important at higher energies), and (d) the neglect of other possible degrees of freedom beyond 150 MeV such as, for example, the role of the pion-production and isobar-formation channels. It is, in part, with these uncertainties regarding previous studies in mind that the extensive measurements and the comprehensive analysis reported in this paper were undertaken.

The experimental procedures for data acquisition and aspects of data reduction are briefly described in Sec. II, the procedures and the results of the optical-model analysis are presented in Sec. III, and features of the data, interpretations of the optical-model results, and comparisons with

microscopic models are discussed in Sec. IV. The conclusions and a brief summary are given in Sec. V.

## II. EXPERIMENT

### A. Procedure

The cross section measurements reported here were made using 80–180 MeV proton beams from the Indiana University Cyclotron Facility (IUCF). The scattered protons were detected and identified using a quadrupole-dipole-dipole-multipole (QDDM) magnetic spectrograph<sup>17</sup> (with a momentum acceptance of 3%) employing an array of detectors on its focal plane. The first element of the array was a 60-cm long position-sensitive, helical-wire ionization chamber for momentum information. This was normally followed by two closely spaced, large plastic scintillators (7 and 12 mm thick) which served as energy loss detectors for particle identification. Real events in the detector array were determined by a fast triple coincidence requirement. This combination of magnets and detectors provided energy information with overall resolution of better than  $10^{-3}$  and unique particle identification over the dynamic range of the spectrograph. The addition of lead and concrete shielding near the focal plane reduced the rate due to general room background (arising largely from neutron-induced recoil protons) to an elastic cross-section equivalent of  $\lesssim 1 \mu\text{b}/\text{sr}$ . To measure cross sections down to a few nb/sr (e.g., at large angles,  $\theta \gtrsim 80^\circ$ ) the background contribution was further reduced by employing narrow scintillators covering only 20% of the focal plane. In addition, these scintillators were separated by 40 cm to appreciably reduce their relative solid angle, and time-of-flight requirements were added to the event discrimination.

The targets used in these measurements were self-supporting foils of 99.14% isotopically pure <sup>208</sup>Pb, 97.65% <sup>90</sup>Zr, and natural calcium (96.9% <sup>40</sup>Ca). The thicknesses ranged from about 4 to 32 mg/cm<sup>2</sup>. The size of the beam spot on target was generally  $3 \times 3 \text{ mm}^2$ . The beam intensity on target varied from a fraction of a nA to 400 nA, depending upon the scattering angle, and was controlled to keep the singles counting rates in the various detectors below about 10 kHz and/or to keep the composite dead time due to counter electronics, PACE data acquisition system, and computer to below 10%. The overall system dead time was monitored by feeding pulses from a pulser, triggered at a rate proportional to the beam current, into all detectors and processing the signals in the same manner as those from real

events in the detectors.

The measurements reported here were made at nominal energies of 80, 135, and 160 MeV for  $^{40}\text{Ca}$ , at 80, 135, 160, and 180 MeV for  $^{90}\text{Zr}$ , and at 80, 121, 160, and 182 MeV for  $^{208}\text{Pb}$ . The overall energy resolution  $\Delta E$  was typically 100–150 keV, and the uncertainty in bombarding energy was comparable to  $\Delta E$ . The measurements generally covered an angular range in the laboratory from  $6^\circ$  to  $81^\circ$ – $93^\circ$  in  $0.5^\circ$  steps (depending on target, energy, and angle region), with the exception of  $^{90}\text{Zr}$  at 135 MeV where the angular range was extended to  $126^\circ$ . The relative errors associated with the measured cross sections arose mainly from the following known sources: (a) counting statistics, which typically were less than 1–2% but rarely larger than 10%; (b) uncertainty in the dead time, which was kept below 1%; (c) uncertainty in charge collection, estimated to contribute up to 1% at low beam currents (i.e., at forward angles); (d) uncertainties in effective scattering angle due to variation in beam direction during measurements, angle setting, and readout errors (including possible nonlinearity of the angle scale), and uncertainty in the nominal  $0^\circ$  reference (the latter was checked for each target and energy by measuring on both sides of  $0^\circ$ ). The combined angle error was estimated to be  $\pm 0.03^\circ$ ; the corresponding cross section errors ranged from negligible to as high as 7%, depending on the slope of the cross section at a given angle. The level of reproducibility of measurements indicated the presence of additional relative errors of about 1% from other (unknown) sources. The relative errors from all sources were combined in quadrature to obtain the total relative error which was typically 2–3% at angles forward of about  $60^\circ$ . The total systematic (normalization) error, arising from uncertainties in target thickness, charge integration, target angle, and spectrograph solid angle, was estimated to be about 8–10%. Details of the experimental method and the data reduction can be found elsewhere.<sup>18</sup> Tabulations of the cross section data can be obtained from the authors at IUCF.

### B. Data

In Fig. 1 we compare the present differential cross-section measurements  $\sigma(\theta)$  at 160- and 180-MeV proton energy for  $^{40}\text{Ca}$ ,  $^{90}\text{Zr}$ , and  $^{208}\text{Pb}$  to the previous data<sup>9–12</sup> at these energies. In Fig. 2 the IUCF measurements for  $^{40}\text{Ca}$ ,  $^{90}\text{Zr}$ , and  $^{208}\text{Pb}$  are presented along with previous data at other energies between 61 and 182 MeV.<sup>7,8,12</sup> The curves in Fig. 1 are drawn through the IUCF data points as guides for the eye, while the curves in Fig. 2 represent the results of optical-model cal-

culations discussed in later sections of this paper.

The comparison of present results with earlier work in Fig. 1 is meant to call attention to two noteworthy points: First, there is a considerably greater range in scattering angle, and consequently greater range in magnitude of the cross sections (up to 9 decades), encompassed by the present measurements. Second, one notes some small but nevertheless significant differences in shape and normalization between the old and new 160-MeV angular distributions. In Fig. 2, which displays the cross sections as ratio-to-Rutherford on a logarithmic scale, the systematic trends of the data with energy and target can be noted. Characteristic diffraction of the proton waves by the target nucleus is observed; the decrease in spacing of diffraction minima with increasing target radius  $R$  and wave number  $k$  (in accordance with  $\Delta\theta \sim \pi/kR$ ), and the increase in average falloff of  $\sigma(\theta)$  with increasing  $R$  and  $k$  (classical diffraction theory predicts  $\ln\sigma(\theta) = \text{const} - \gamma\theta$ , with  $\gamma \propto (kR)^{1/3}$ ). The onset of damping of these diffractive oscillations over the mid-angle range, observed for the first time in the present measurements, is a characteristic feature of all targets and is seen to occur at higher bombarding energies for a larger target mass, e.g., above 100 MeV for  $^{40}\text{Ca}$ , above 135 MeV for  $^{90}\text{Zr}$ , and above 160 MeV for  $^{208}\text{Pb}$ . At much higher energies (e.g., 613 MeV and beyond) the cross section angular distributions again exhibit very regular diffraction structure similar to that observed below 100–120 MeV. This damping phenomenon is thus peculiar to the energy region  $100 \lesssim E_p \lesssim 300$  MeV, as one can demonstrate<sup>24</sup> by optical model calculations of  $\sigma(\theta)$  using potentials based on the available cross section data between 60 MeV and 1 GeV.

In a plot of the cross section  $\sigma(q)$  as a function of momentum transfer,  $q = 2k \sin(\theta/2)$ , one also notes that associated with the onset of damping in the region  $1.8 < q < 2.8 \text{ fm}^{-1}$  is a reduction in the number of diffraction minima (from 9 to 8 for the data range  $q < 4 \text{ fm}^{-1}$ ) in going from proton energies below 150 MeV to energies above 250 MeV. This change in diffraction structure implies a decrease in the effective radial extent of the nuclear potential with increasing energy which may be qualitatively understood in terms of a progressive reduction in the Pauli suppression of the potential in the nuclear interior coupled with a reduction in the range of the fundamental two-nucleon interaction.

## III. ANALYSIS

### A. General

The differential cross section data for  $^{40}\text{Ca}$ ,  $^{90}\text{Zr}$ , and  $^{208}\text{Pb}$  obtained at IUCF were combined with

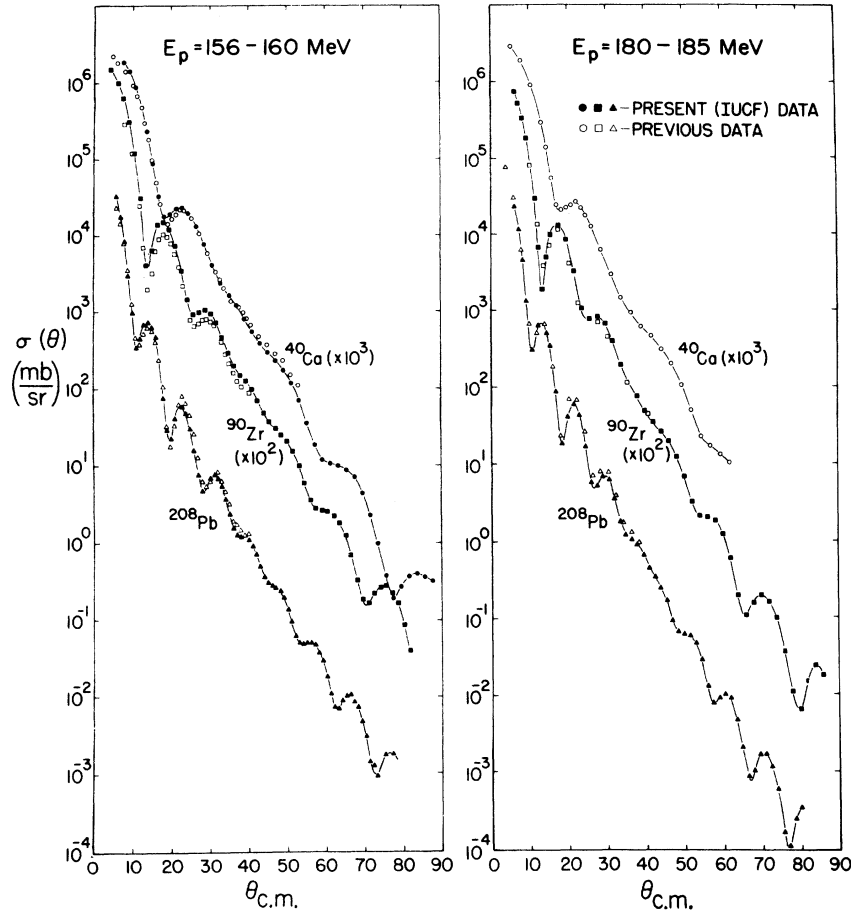


FIG. 1. Comparison of present measurements of differential cross section angular distributions (solid symbols) with previous data (open symbols) in the energy regions 156–160 MeV (Ref. 9) and 180–185 MeV (Refs. 11 and 12). The curves drawn through the present data points are guides to the eye only.

existing data for these targets from ORNL<sup>7</sup> at 61.4 MeV, from Maryland<sup>8</sup> at 100.4 MeV, and from Uppsala<sup>12</sup> at 181 MeV to form a sufficiently extensive data set for a global analysis of proton elastic scattering between about 60 and 180 MeV.

In view of the general lack of associated polarization data  $P(\theta)$  of quality comparable to that of the differential cross sections  $\sigma(\theta)$  at the time this analysis was undertaken, the primary emphasis of the analysis was placed on a systematic and consistent description of the cross section data alone in terms of a phenomenological optical model (OM). For those particular nuclei and energies where  $P(\theta)$  data were available,<sup>11,12,19,20</sup> an analysis was also subsequently carried out on the combined set of  $\sigma(\theta)$  and  $P(\theta)$  data to more reliably establish the systematic behavior of the spin-orbit potential with energy and target mass. Towards the conclusion of the analysis program, preliminary results from new  $P(\theta)$  measurements between 80 and 180 MeV became available<sup>21</sup> to provide

further constraints on the spin-orbit interaction, permitting us to establish finally a realistic, average, global parametrization of the proton-nucleus optical potential at medium energies (up to about 200 MeV).

#### B. Optical-model potential and wave equation

Using the code **SNOOPY**,<sup>22</sup> angular distributions were fit with a local, complex, spin-dependent OM potential of conventional form, containing a Coulomb term, a complex nuclear central term, and a complex nuclear spin-orbit (SO) term:

$$U(r) = U_{\text{Coul}}(r) - Vf_0(r) - i \left( W_s - 4a_w W_D \frac{d}{dr} \right) f_w(r) + 2(V_{\text{so}} + iW_{\text{so}}) \frac{1}{r} \frac{d}{dr} f_{\text{so}}(r) \vec{L} \cdot \vec{\sigma} \quad (1)$$

with Woods-Saxon (WS) form factors  $f_x(r; r_x, a_x)$  and 10 free parameters. The factor 2 multiplying the SO term is the conventional pion Compton wave-

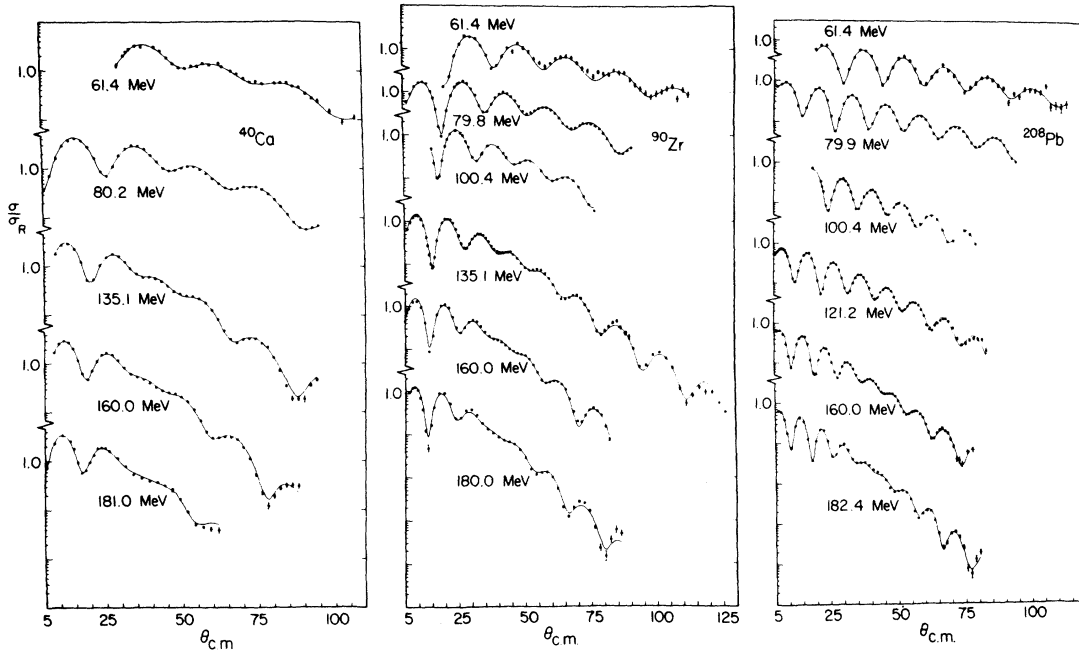


FIG. 2. Differential cross section angular distributions plotted as ratio-to-Rutherford for  $^{40}\text{Ca}$  from 61.4 MeV to 181 MeV (61.4-MeV data from Ref. 7, 181-MeV data from Ref. 12); for  $^{90}\text{Zr}$  from 61.4 MeV to 180 MeV (61.4-MeV data from Ref. 7, 100.4-MeV data from Ref. 8); and for  $^{208}\text{Pb}$  from 61.4 to 182.4 MeV (61.4-MeV data from Ref. 7, 100.4-MeV data from Ref. 8). Relative errors are indicated where they exceed the size of the symbols (approximately  $\pm 5\%$ ). The curves represent 10-parameter optical-model fits to the data.

length factor  $(\hbar/m_\pi c)^2$  in  $\text{fm}^2$ . Note that common geometries were employed for the real and imaginary SO terms and for the volume and surface-peaked central absorption terms; only for the 61.4-MeV data were both absorptive terms,  $W_S$  and  $W_D$ , required for a good fit.

The analysis was carried out with a semirelativistic generalization of the conventional nonrelativistic Schrödinger formulation of the scattering process. Relativistic kinematics were used for the projectile, but it was assumed that the target motion in the center-of-mass frame could be treated nonrelativistically at proton energies below 200 MeV for the target masses considered here ( $A \geq 40$ ). A relativistic Schrödinger-type wave equation was generated by appropriate reduction of the Dirac equation for a massive, energetic fermion (mass  $m$ , c.m. wave number  $k$ ) moving in a localized central potential field  $U(r)$ . The potential  $U(r)$  was chosen to be the fourth (time-like) component of a Lorentz vector potential, satisfying the conditions  $U \ll m$ , and  $\nabla U/U \ll k$ , both good approximations for intermediate-energy proton scattering. In the reduced 2-body problem with relativistic projectile but nonrelativistic target (mass  $M$ ) the large component of the partial wave function  $F_L(\rho)$  can be shown to satisfy the radial equation

$$\left[ \frac{d^2}{d\rho^2} + \left( 1 - \frac{\tilde{U}(\rho)}{E - M - m} - \frac{L(L+1)}{\rho^2} \right) \right] F_L(\rho) = 0, \quad (2a)$$

with  $\rho = kr$ , where  $k = (M/E)[T(T+2m)]^{1/2}$ ,  $T$  is the projectile laboratory kinetic energy, and  $E$  denotes the total energy of the system in the c.m. frame. Equation (2a) is seen to have the form of a conventional nonrelativistic Schrödinger equation but with relativistic kinematic variables (in units where  $\hbar = c = 1$ ) and a renormalized total (Coulomb + nuclear) OM potential:

$$\tilde{U} = \gamma U, \quad \gamma = \frac{2(E - M)}{E - M + m}. \quad (2b)$$

The spin-orbit term in  $U(r)$  employed in this analysis is a purely phenomenological one since the intrinsic SO term in the Dirac equation is negligibly small in the above limits.

### C. Analysis procedure and fits to the data

Initially all 10 parameters ( $V$ ,  $r_0$ ,  $a_0$ ,  $W_S$ ,  $r_w$ ,  $a_w$ ,  $V_{s0}$ ,  $W_{s0}$ ,  $r_{s0}$ , and  $a_{s0}$ ) of the optical potential were varied in unconstrained "best-fit" searches on the data. In general, allowing the SO parameters to vary freely in fitting  $\sigma(\theta)$  data leads to substantial parameter ambiguities for both SO and central potentials. However, preliminary studies with the present  $\sigma(\theta)$  data base indicated

an unusual sensitivity to the spin dependence of the OM potential at those energies where the damping of the oscillatory structure in  $\sigma(\theta)$  is observed. It was therefore considered useful to determine to what extent, if any, an unconstrained analysis of the  $\sigma(\theta)$  data could provide information on the energy systematics of the complex SO potential, and its corresponding volume integrals, for  $E_p = 60\text{--}180$  MeV. These unconstrained parameter searches were also meant to provide a benchmark for the quality of "best fits" obtainable with the new, high-precision medium-energy data for comparison with subsequent fits to be obtained under various parameter constraints.

Next, "fixed-geometry," 6-parameter searches were carried out on the  $\sigma(\theta)$  data in which the geometrical parameters  $r_0$ ,  $a_0$ ,  $r_w$ , and  $a_w$ , of the complex central potential were constrained to energy-averaged values for a given nucleus. The purpose here was to establish general trends of the central potential strengths  $V$  and  $W_s$  with energy and target mass. The particular average geometrical parameters employed in this phase of the analysis are by no means unique since free adjustment of the SO parameters appears to be capable of compensating for rather wide variations in central potential parameters when fitting only  $\sigma(\theta)$  data. Furthermore, the optical potential obtained at this stage, while providing excellent fits to the  $\sigma(\theta)$  data, in many cases failed to give an acceptable reproduction of the available  $P(\theta)$  data.

Finally, in the third phase of the analysis, we constrained the SO parameters to the constant geometry values and energy- and target-dependent strengths indicated by a preliminary analysis<sup>21</sup> of the new  $P(\theta)$  data. Only with this last prescription did we arrive at a consistent and systematic global OM parameter set for  $E_p = 80\text{--}180$  MeV which provides a good overall description of the observables  $\sigma(\theta)$  and  $P(\theta)$ . However, nearly all parameters of this "fixed-SO" set exhibit significant energy- and target-mass dependence.

In the following subsections (III C 1 through III C 3) these three phases of the OM analysis are described in more detail. The principal features of the results of these analyses and their interpretation are discussed in Sec. IV.

### 1. Best-fit searches

The overall quality of the 10-parameter fits to the total set of cross section data was excellent over the whole angular range, in terms of the usual objective  $\chi^2$  criterion, as well as by visual comparison of data points and calculated curves. The numerical results of this best-fit analysis are listed in Table I, and the fits are presented graphically in Fig. 2.

In Table I we list all potential volume integrals and the reduced  $\chi^2$  values ( $\chi^2$  normalized by the number of data points). Since the average value of  $\chi^2/N$  for all data is about 3.7 and since the average relative error in the data is roughly  $\pm 3\%$ , the average rms deviation between the fitted curve and the measurements is approximately  $\pm 6\%$ . We do not list the individual potential parameter values for each energy  $E_p$  and target mass  $A$  because of their lack of uniqueness and considerable scatter with  $E_p$  and  $A$  (a more physically meaningful, constrained parameter set is described in Sec. III C 3). However, volume integrals and rms radii are relatively less affected by common parameter ambiguities and correlations. Hence, these quantities may more readily exhibit systematic trends and can thus facilitate comparison with results of microscopic calculations of the optical potential. The normalized volume integrals (per unit nucleon mass) listed in Table I for both the real and imaginary parts of the central and spin orbit potentials, are defined as

$$K \equiv \begin{cases} J/A, & \text{for central potentials} \\ J/A^{1/3}, & \text{for SO potentials} \end{cases} \quad (3a)$$

with

$$J \equiv \int_0^\infty 4\pi \bar{U}(r) r^2 dr, \quad (3b)$$

where  $\bar{U}(r)$  is the appropriate renormalized nuclear potential (central or SO, real or imaginary part) including the factor  $\gamma$  defined by Eq. (2b). For the potential of Eq. (1) with WS form factors the real volume integrals  $J_R$ , for example, can be evaluated approximately to order  $(a/R)^2$  as

$$J_R \equiv \begin{cases} \frac{4}{3} \pi R_0^3 V_0 [1 + (\pi a_0/R_0)^2] \\ = A \cdot \frac{4}{3} \pi r_0^3 V_0 [1 + (\pi a_0/R_0)^2] & \text{(central)} \\ 8\pi V_{so} R_{so} = A^{1/3} \cdot 8\pi V_{so} r_{so} & \text{(SO)} \end{cases} \quad (4)$$

These relations exhibit explicitly the different  $A$  dependences of the central and SO volume integrals which were divided out in Eq. (3a). Also listed in Table I are the rms radii,  $R \equiv \langle r^2 \rangle^{1/2}$ , for the real and imaginary parts of the central and SO potentials, as well as the calculated OM reaction cross section  $\sigma_R$ .

In the six cases where  $P(\theta)$  data<sup>11,12,19,20</sup> existed at the same or nearby energies to the  $\sigma(\theta)$  data, both types of data were also analyzed for the best simultaneous fit in a free (10-parameter) search. Where necessary, the polarization data were transformed to an energy equivalent to the cross section measurements by shifting the  $P(\theta)$  scattering angles so as to retain the same momentum transfer when calculated at the  $\sigma(\theta)$  energy. The result-

TABLE I. Normalized volume integrals ( $\text{MeV fm}^3$ ), rms radii (fm), and reaction cross section (mb) for the 10-parameter optical potential providing the best fit to cross section data. The values at energies labeled by an asterisk are results for best simultaneous fit to cross section and polarization data.

Target, energy (MeV)	$\frac{\chi_o^2}{N_o}$	$\frac{\chi_p^2}{N_p}$	$\gamma$	Data Ref. <sup>a</sup>	$K_R^c$	$R_R^c$	$K_I^c$	$R_I^c$	Spin-orbit potential			$\sigma_R$
									$K_R^{so}$	$R^{so}$	$K_I^{so}$	
<sup>40</sup> Ca	61.4	1.4	1.031	b	345.5	4.235	104.7	4.800	145.4	4.058	-36.4	736
	80.2	4.3	1.040	pres. expt.	300.6	4.341	100.9	4.258	93.1	3.898	-65.3	593
	135.1	4.9	1.066	pres. expt.	197.2	4.200	114.7	4.279	99.9	4.060	-25.1	562
	160.0	3.6	1.077	pres. expt.	194.6	4.299	97.3	4.313	85.3	4.147	-29.9	479
	160*	4.7	3.7	e (153 MeV)	202.0	4.302	127.3	4.167	77.0	3.871	-46.2	548
	181	4.7	1.086	c	194.6	4.167	114.7	4.450	88.0	4.131	-44.0	517
	181*	7.8	9.0	f (175 MeV)	236.9	4.388	86.1	4.352	63.1	4.134	-56.8	400
<sup>90</sup> Zr	61.4	2.0	1.031	b	315.2	4.856	87.5	5.987	169.6	5.671	-42.4	1183
	62*	3.8	7.9	g (65 MeV)	342.2	5.005	90.6	5.671	138.1	5.314	-14.4	1213
	79.8	5.0	1.040	pres. expt.	289.8	5.062	85.9	5.273	87.0	5.073	-52.3	1023
	100.4	1.3	1.050	d	249.8	5.059	85.6	5.308	85.5	5.152	-49.6	958
	135.1	4.2	1.066	pres. expt.	223.6	5.030	116.6	5.215	96.5	5.145	-43.3	1036
	160.0	5.9	1.078	pres. expt.	225.2	5.101	109.0	5.253	99.7	5.338	-34.0	971
	179.9	6.1	1.087	pres. expt.	206.6	5.230	85.1	5.174	64.0	5.255	-38.5	799
	180*	6.3	15	h (185 MeV)	218.6	5.285	65.8	5.135	41.5	5.275	-50.0	650
<sup>208</sup> Pb	61.4	1.3	1.032	b	326.5	5.948	116.0	7.441	136.3	7.035	-40.8	2024
	79.9	3.3	1.041	pres. expt.	278.3	6.089	102.9	6.811	147.3	6.810	-29.4	1982
	100.4	3.0	1.051	d	273.5	6.147	85.2	6.685	124.4	6.724	0	1790
	121.2	3.3	1.060	pres. expt.	217.3	6.336	89.4	6.545	109.6	6.856	-27.5	1712
	160.0	4.0	1.078	pres. expt.	198.6	6.303	81.6	6.679	51.0	6.997	-30.6	1580
	160*	4.8	14	j, e (153 MeV)	201.8	6.385	75.9	6.650	46.8	6.935	-37.3	1512
	182.4	4.6	1.088	pres. expt.	202.8	6.374	79.5	6.628	48.6	7.044	-29.2	1511
	182*	8.9	32	k (185 MeV)	207.8	6.399	78.6	6.619	41.0	7.028	-37.0	1489

<sup>a</sup>Where necessary, polarization data was scaled to the energy of cross section measurements (column 1) by adjusting the scattering angles to correspond to the same momentum transfer at the two energies.

<sup>b</sup>C. B. Fulmer, J. B. Ball, A. Scott, and M. L. Whiten, Phys. Rev. **181**, 1565 (1969).

<sup>c</sup>A. Ingemarsson and G. Tibell, Phys. Scr. **4**, 235 (1971).

<sup>d</sup>K. Kwiatkowski and N. S. Wall, Nucl. Phys. **A301**, 349 (1978).

<sup>e</sup>C. Rolland *et al.*, Nucl. Phys. **80**, 625 (1966).

<sup>f</sup>P. Hillman, A. Johansson, and H. Tyren, Nucl. Phys. **4**, 648 (1957).

<sup>g</sup>M. Nakamura *et al.*, RCNP Annual report, Osaka University, 1977, p. 129.

<sup>h</sup>E. Hagberg, A. Ingemarsson, and B. Sundqvist, Phys. Scr. **3**, 245 (1971).

<sup>j</sup>A. Willis *et al.*, J. Phys. **30**, 13 (1969).

<sup>k</sup>W. T. H. van Oers *et al.*, Phys. Rev. C **10**, 307 (1974).

ing fits to the  $P(\theta)$  data are illustrated in Fig. 3 and the potential volume integrals and rms radii are listed in Table I for the energies indicated by asterisks. Fits to the  $\sigma(\theta)$  data were not perceptively different from those displayed in Fig. 2. While for  $P(\theta)$  the agreement with measurement is qualitatively acceptable in all cases, the fits are reasonably good only for <sup>90</sup>Zr at 62 MeV, <sup>40</sup>Ca at 160 MeV, and <sup>90</sup>Zr at 180 MeV. By comparing the corresponding entries in Table I we note that the simultaneous fits to both  $\sigma(\theta)$  and  $P(\theta)$ , compared to fitting  $\sigma(\theta)$  only, altered the SO parameters as well as the central potential parameters somewhat. These changes, however, are within the range of parameter uncertainties and parameter correlations.

A difficulty encountered for certain cases in the simultaneous OM analysis of  $\sigma(\theta)$  and  $P(\theta)$  data was

evidenced by the fact that a *common* set of potential parameters giving acceptable fits to each type of data could not be found. For <sup>208</sup>Pb at 160 and 182 MeV, and for <sup>90</sup>Zr at 180 MeV, considerably different sets of parameters were required to obtain best fits for  $\sigma(\theta)$  and  $P(\theta)$  separately. In these three cases, the fits to  $\sigma(\theta)$  indicate smaller values of the ratio of imaginary-to-real SO strength  $\epsilon = W_{so}/V_{so}$  (-0.6 to -0.7) while fits to  $P(\theta)$  point to values of  $\epsilon$  larger by about a factor of 2 (-1.0 to -1.6). These are also the cases which give the lowest values for the real spin orbit potential volume integral.

## 2. Fixed-geometry searches

The results of fitting the differential cross sections with a 6-parameter, constrained-geometry model are presented in Table II. In these fits the

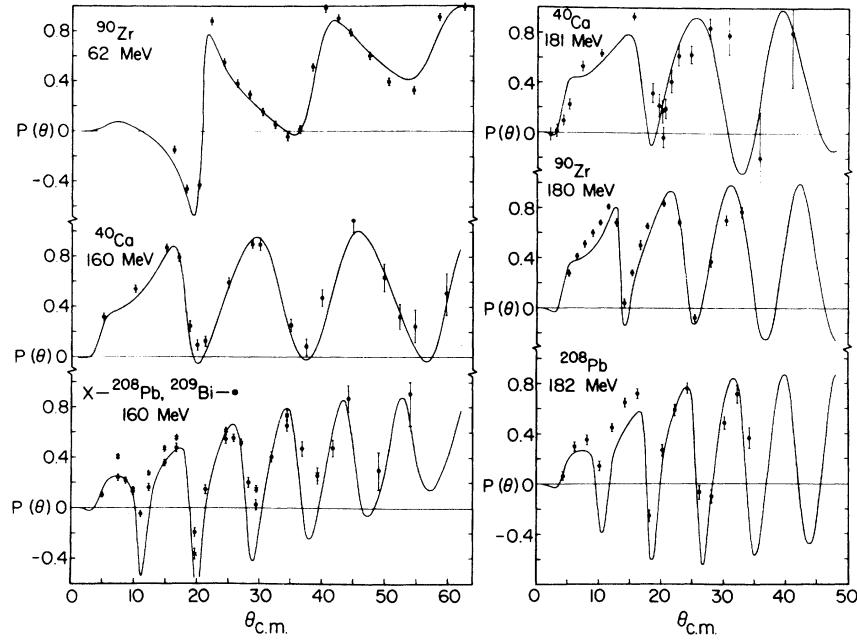


FIG. 3. Polarization data for  $^{40}\text{Ca}$ ,  $^{90}\text{Zr}$ , and  $^{208}\text{Pb}$  from 62 MeV to 182 MeV (Ref. 11, 12, 19, and 20). The curves are optical-model fits from simultaneous searches on cross sections and polarizations.

geometrical parameters of the real central potential were fixed at the average values

$$r_0 = 1.21 \text{ fm}, \quad a_0 = 0.77 \text{ fm} \quad (5)$$

for all nuclei, while the geometrical parameters  $r_w, a_w$  of the imaginary central potential were fixed for each nucleus (mass number  $A$ ) at values given by the relations

$$\begin{aligned} r_w &\approx 1.37 + 3.5 A^{-1} (\text{fm}), \\ a_w &\approx 0.36 + 0.036 A^{1/3} (\text{fm}). \end{aligned} \quad (6)$$

The quality of the fits to the data with these constrained geometries is still subjectively quite good, though the average value of  $\chi^2/N = 8.5$  is a factor of 2.5 larger than that for the free-search fits; in a few cases  $\chi^2/N$  increased by as much as

TABLE II. Normalized volume integrals ( $\text{MeV fm}^3$ ), rms radii (fm), and reaction cross sections (mb) for the 6-parameter, fixed-geometry fits to cross section data.

Target, energy (MeV)	$\frac{\chi_R^2}{N_O}$	$K_R^c$	Central potential			Spin-orbit potential				$\sigma_R$
			$R_R^c$	$K_I^c$	$R_I^c$	$K_R^{so}$	$R^{so}$	$K_I^{so}$		
$^{40}\text{Ca}$	61.4	1.8	327.7	4.297	71.2	4.258	107.2	4.079	-26.9	576
	80.2	10.5	305.9	4.297	101.7	4.258	86.8	3.808	-48.8	613
	135.1	8.2	200.6	4.297	116.6	4.258	105.7	4.102	-21.0	567
	160.0	7.4	190.0	4.297	113.8	4.258	98.0	4.165	-14.6	533
	181	10.8	187.2	4.297	103.4	4.258	98.2	4.135	-34.2	473
$^{90}\text{Zr}$	61.4	2.1	321.7	5.083	80.1	5.263	100.3	5.379	-50.1	1121
	79.8	13.1	295.0	5.083	85.1	5.263	63.0	4.894	-47.3	1029
	100.4	3.4	257.0	5.083	88.3	5.263	78.4	5.002	-46.6	977
	135.1	9.3	218.7	5.083	119.5	5.263	93.1	5.247	-56.0	1044
	160.0	10.8	216.9	5.083	99.4	5.263	93.0	5.266	-32.6	927
179.9	21.0	209.6	5.083	76.4	5.263	78.7	5.346	-19.7	773	
$^{208}\text{Pb}$	61.4	2.4	316.3	6.247	74.4	6.722	148.8	6.968	-7.3	2001
	79.9	9.3	265.2	6.247	96.9	6.722	145.3	6.849	-50.8	1904
	100.4	3.7	266.0	6.247	75.0	6.722	115.0	6.823	-8.0	1711
	121.2	6.7	246.2	6.247	89.3	6.722	93.7	6.826	-29.8	1764
	160.0	9.6	218.0	6.247	83.0	6.722	65.4	6.976	-23.3	1619
	182.4	16.7	203.2	6.247	84.1	6.722	52.8	7.063	-27.3	1577

a factor of 3.5. Hence the average rms deviation between calculation and experiment is still within  $\pm 10\%$ .

Considerable differences are found in many cases between the values of the corresponding volume integrals for the best-fit and fixed-geometry results for  $\sigma(\theta)$ . This is indicative of the degree of interplay and compensating behavior possible among the four nuclear potential terms when fitting cross-section data alone at medium energies.

### 3. Fixed-spin-orbit searches

In order to remove the considerable degree of freedom allowed the central potential parameters in fitting  $\sigma(\theta)$  data when the SO parameters are free to vary, we constrained the latter in this phase of the analysis in accordance with the average SO geometry and SO volume integrals determined in a preliminary analysis of  $P(\theta)$  data by Schwandt *et al.*<sup>21</sup> These SO quantities, valid over the energy range  $60 < E_p < 200$  MeV, are expressed by the relations ( $E_p$  in MeV):

$$r_{so} = 1.015 + 0.0005A \text{ (fm)}, \quad a_{so} = 0.60 \text{ fm} \quad (7a)$$

$$K_R^{so} = \begin{cases} 400 \pm 4 - 69 \ln E_p, & \text{MeV fm}^3 \text{ for } {}^{40}\text{Ca} \\ 430 \pm 4 - 71 \ln E_p, & \text{MeV fm}^3 \text{ for } {}^{90}\text{Zr} \\ 470 \pm 4 - 74 \ln E_p, & \text{MeV fm}^3 \text{ for } {}^{208}\text{Pb} \end{cases} \quad (7b)$$

$$K_I^{so} = 145 \pm 4 - 38 \ln E_p, \quad \text{MeV fm}^3. \quad (7c)$$

The real and imaginary SO strength parameters  $V_{so}, W_{so}$  are readily obtained from these relations using Eq. (4). With the SO potential thus con-

strained, 6-parameter searches for the central potentials were carried out. A smooth, monotonic variation with energy was observed for most of the parameters resulting from this fitting process. The geometrical parameters  $r_0$  and  $a_w$  were particularly well defined and were represented by relations linear in energy ( $E_p$  in MeV):

$$r_0 = 1.18 + (0.34 + 6.5A^{-1}) \times 10^{-3} E_p, \quad (8)$$

$$a_w = 0.37 + 1.8 \times 10^{-3} E_p$$

in subsequent 4-parameter searches for  $V, a_0, W_s,$  and  $r_w$ . On the basis of these latter searches, we were also able to fix the diffuseness parameter  $a_0$  to values given by the relation ( $E_p$  in MeV)

$$a_0 = 0.77 + 1.2 \times 10^{-4} A^{0.4} (180 - E_p). \quad (9)$$

With  $r_0, a_0,$  and  $a_w$  thus fixed, the final values of the strengths  $V, W_s,$  and the radius parameter  $r_w$  were determined in 3-parameter searches on  $\sigma(\theta)$ .

These "fixed-SO" parameters are listed in Table III, along with the potential volume integrals and rms radii. All potential parameters are graphically presented in Fig. 4. The average value of  $\chi^2/N$  (11.5), is only slightly worse than that for the "fixed geometry" analysis (Sec. III C 2); the average rms deviation between OM calculation and data is about 10%. While the constraint relations (8) and (9) for the central geometry parameters cannot be considered unique, they are consistent with the general systematics also present in the parameter sets from the "best-fit" and "fixed-geometry" searches, namely,  $r_{so} < r_0 < r_w, a_0 > a_w,$

TABLE III. Potential parameters  $V, W,$  and  $r_w,$  normalized volume integrals ( $\text{MeV fm}^3$ ), rms radii (fm), and reaction cross sections  $\sigma_R$  (mb) for the 3-parameter, fixed-spin-orbit fits to cross section data.

Target energy (MeV)	$\chi_\sigma^2/N_\sigma$	$V$ (MeV)	$W_s(W_D)$ (MeV)	$r_w$ (fm)	$K_R^c$	Central potential				Spin-orbit potential			$\sigma_R$
						$R_R^c$	$K_I^c$	$R_I^c$		$K_R^{so}$	$R^{so}$	$K_I^{so}$	
${}^{40}\text{Ca}$	61.4	6.0	33.0	5.46(1.44)	1.445	315.6	4.151	97.1	4.487	139.4	4.016	-10.7	688
	80.2	3.8	30.2	6.66	1.470	296.7	4.195	97.6	4.331	123.0	4.016	-20.3	618
	135.1	15.0	22.0	6.82	1.445	229.9	4.274	99.7	4.455	90.1	4.016	-40.2	522
	160.0	11.9	20.3	7.54	1.367	222.5	4.372	96.2	4.362	78.4	4.016	-46.2	469
	181.0	9.3	17.45	9.56	1.255	195.6	4.416	99.3	4.199	70.6	4.016	-50.8	442
${}^{90}\text{Zr}$	61.4	7.5	36.9	5.67(2.17)	1.400	312.4	4.883	92.7	5.575	138.7	5.115	-9.6	1200
	79.8	23.8	31.9	7.80	1.414	275.9	4.936	98.2	5.261	120.4	5.115	-20.8	1109
	100.4	6.6	27.9	7.46	1.404	247.8	4.988	92.9	5.285	103.4	5.115	-29.4	1020
	135.1	7.9	23.9	7.73	1.380	221.6	5.082	93.3	5.297	83.8	5.115	-39.8	950
	160.0	17.0	22.3	8.46	1.330	212.2	5.157	93.3	5.219	71.8	5.115	-45.9	878
179.9	10.0	19.4	10.05	1.270	189.6	5.204	98.7	5.098	63.7	5.115	-50.6	853	
${}^{208}\text{Pb}$	61.4	5.2	39.8	7.17(1.75)	1.420	312.1	6.014	103.3	7.052	138.0	6.903	-10.2	2038
	79.9	17.1	34.6	7.40	1.448	276.8	6.077	97.2	6.909	115.7	6.903	-20.5	1961
	100.4	18.4	30.2	7.78	1.415	247.6	6.142	96.3	6.810	96.2	6.903	-29.5	1881
	121.2	4.1	27.1	8.37	1.400	227.7	6.202	101.0	6.784	82.0	6.903	-40.3	1853
	160.0	12.7	22.1	8.95	1.345	194.0	6.333	97.0	6.635	59.2	6.903	-47.0	1690
	182.4	19.2	21.4	10.77	1.270	192.3	6.398	99.0	6.366	39.8	6.903	-50.5	1595

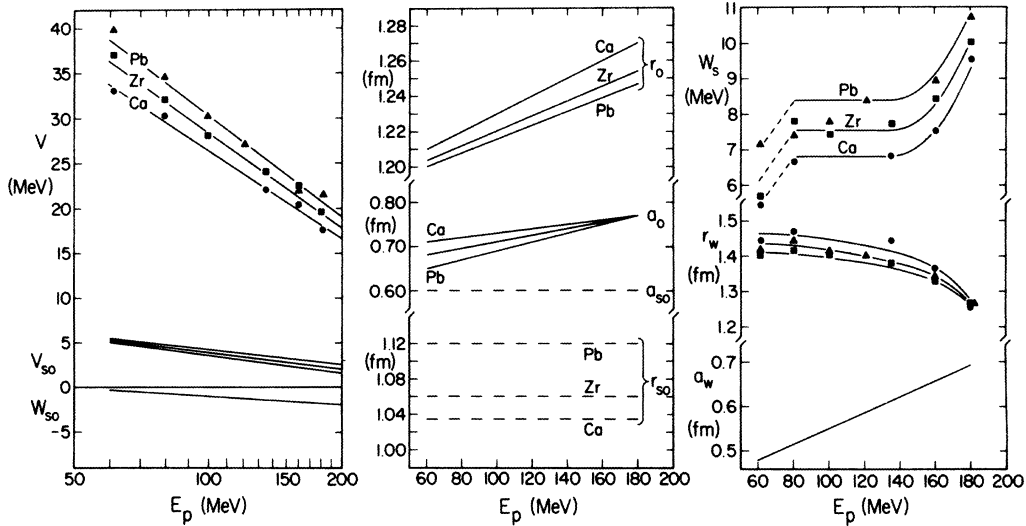


FIG. 4. Energy dependence of the complex central and spin-orbit potential parameters obtained in the fixed-spin-orbit fits to cross section data. The lines represent the analytical expressions of Eqs. (16a)–(16c). Note the logarithmic energy scale in the left-hand panel.

and  $r_0$ ,  $a_0$ ,  $a_w$  increasing with energy. The average dependence of these parameters on target mass  $A$  is relatively weak.

Aside from substantially reducing the scatter (with  $E_p$  and  $A$ ) in the potential parameters obtained in the two preceding analyses, the most significant consequence of constraining the SO parametrization was to make the central potential geometry parameters energy dependent. In particular, the radius of the real central potential was forced to increase with energy, from a value of about  $1.19A^{1/3}$  fm around 40 MeV to values in the range  $(1.25\text{--}1.27)A^{1/3}$  fm near 180 MeV. Some evidence for this behavior was seen already in the results of the best-fit analysis. The low-energy value is reasonably consistent with that of the popular Becchetti-Greenlees global potential<sup>23</sup> for  $E_p < 50$  MeV ( $1.17 A^{1/3}$  fm); an OM analysis of higher-energy data<sup>24</sup> indicates that beyond 200 MeV the radius decreases again with increasing energy. Attempts to fit the 160–180 MeV data with the low-energy value for the radius parameter failed badly. The increase in radius with energy up to 200 MeV of course implies a corresponding increase in rms radius of the real central potential and a somewhat more rapid falloff with energy of the real central strength  $V$ .

#### D. Parameter uncertainties and correlations

In order to obtain some quantitative information about ambiguities and uncertainties in potential parameters, we investigated the variation in the values of the various parameters with changes in angular range and normalization of the data for a few representative cases.

The optical-model code used yields parameter uncertainties and correlation coefficients defined in terms of the conventional error (or correlation) matrix  $\epsilon$ . For the parameters  $p_j$  of the potential model, the parameter uncertainties  $\Delta p_j$  are given by the diagonal elements of  $\epsilon$  (representing the maximum uncorrelated change in  $p_j$  which results in an increase in  $\chi^2$  by one), while the off-diagonal elements of  $\epsilon$  are the parameter correlation coefficients. For the case of  $^{90}\text{Zr}$  at 135 MeV where  $\sigma(\theta)$  extends to  $\theta = 126^\circ$ , the  $\Delta p_j$  were calculated as a function of angular range by analyzing progressively truncated sets of data. Except for  $\Delta W_s$  which is a particularly strong function of  $\theta_{\text{max}}$ , the parameter uncertainties increase by about a factor of 2 when reducing  $\theta_{\text{max}}$  from  $125^\circ$  to  $50^\circ$ . Further reduction in  $\theta_{\text{max}}$  causes the  $\Delta p_j$  to grow quite rapidly. This quantitative analysis affirms our belief that some of the older measurements of 156 MeV (Ref. 9) and 185 MeV (Refs. 11, 12) are indeed of marginal angular extent for a good determination of the OM parameters. Inspection of the parameter correlation coefficients showed that the most significant correlations involve, not surprisingly, parameters of the SO potential, e.g., the combinations  $(r_{\text{so}}, r_0)$ ,  $(a_{\text{so}}, V_{\text{so}}, a_w)$ , and  $(W_{\text{so}}, r_{\text{so}}, W_s)$ .

The normalization of the data (fixed by the nominal target thickness, spectrograph solid angle, etc.) was not allowed to vary in the preceding analyses. When the sensitivity of the fit to absolute normalization of the cross section data was investigated (again for the case of  $^{90}\text{Zr}$  at 135 MeV), renormalization by as much as  $\pm 20\%$  (resulting in a factor of 2 increase in  $\chi^2$ ) changed the

volume integrals of the real central potential by  $\pm 10\%$  and of the real SO potential by  $\pm 15\%$ .

For proton scattering one does not expect to find the kind of strong localization of the interaction to a particular radial region at a particular energy which one commonly observes for more strongly absorbed projectiles. To investigate the radial region of the real central potential to which the data are most sensitive, a small "notch perturbation" of about 1 fm radial extent (comparable to the reduced de Broglie wavelength for protons at these energies) was introduced into  $V(r)$  and the resultant  $\chi^2$  values calculated as function of radial notch position. Typically the fit is quite sensitive to potential perturbations over a wide radial region ( $r \sim 1-8$  fm for  $^{90}\text{Zr}$  at 135 MeV), indicating that the nucleus is in fact fairly transparent to protons at this energy.

#### IV. DISCUSSION OF RESULTS

##### A. Features of the data and interpretation

The most unusual feature of the data at medium energies, as indicated in Sec. II B, is the damping of the diffractive oscillations in the mid-angle range of the forward hemisphere, followed by the reappearance of oscillatory structure at larger angles. Both lower- and higher-energy data, as well as model calculations of angular distributions, show that this phenomenon is essentially restricted to the 100–300 MeV region of proton energies. The general character of polarization  $P(\theta)$  [or analyzing power  $A(\theta)$ ] data over a wide energy range (40–1000 MeV) is that  $P(\theta)$  is positive and large over most of the angular range at both low and high energies, but oscillates strongly (with large negative excursions for heavy nuclei) within precisely the same "transition" energy range of 100–300 MeV over which the damping of  $\sigma(\theta)$  takes place. This suggests a fairly obvious connection between these characteristic features of the  $\sigma(\theta)$  and  $P(\theta)$  distributions through dominance of one spin-channel component of cross section over the other. This conjecture is indeed borne out by direct calculations. At both low and high energies the partial cross section  $\sigma^+$  dominates over  $\sigma^-$  (corresponding to  $\langle \vec{\sigma} \cdot \hat{n} \rangle = \pm 1$ , where  $\hat{n} = \hat{k}_{\text{in}} \times \hat{k}_{\text{out}}$ ) over most of the angular range<sup>25</sup>; consequently the angular structure of  $\sigma(\theta)$  is largely determined by  $\sigma^+$ , and  $P(\theta)$  is positive. In the "transition" region of energy, on the other hand, both  $\sigma^+$ ,  $\sigma^-$  oscillate with comparable amplitudes in the forward hemisphere but with slightly different angular periods (a consequence of the slightly different radii of the total effective nuclear potentials for  $\langle \vec{\sigma} \cdot \hat{n} \rangle = \pm 1$ ; see below). Hence, the oscillations for  $\sigma^+$  and  $\sigma^-$  move out of phase over a portion of

the angular range, leading to a structureless angular distribution for the total differential cross section  $\sigma(\theta) = \sigma^+ + \sigma^-$  and to oscillations in  $P(\theta) \propto \sigma^+ - \sigma^-$ . These characteristic features of  $\sigma^+$ ,  $\sigma^-$  for different bombarding energies are illustrated for  $^{208}\text{Pb}$  in Fig. 5.

The characteristic damping of the  $\sigma(\theta)$  oscillatory structure reflects directly the phasing of  $\sigma^+$ ,  $\sigma^-$  in the transition-energy range, which gives rise to the enhanced sensitivity to the SO potential in the analysis of  $\sigma(\theta)$  data. The complex nature of the SO interaction at these energies is reflected by the elements  $S_L^{J=L \pm 1/2}$  of the scattering matrix. Large SO splitting in the reflection coefficients  $\eta_L^\pm = |S_L^\pm|$  as well as in the real phase shifts  $\delta_L^\pm$  is observed for the surface partial waves corresponding to impact parameters in the radial region of the nucleus where the SO interaction peaks. These

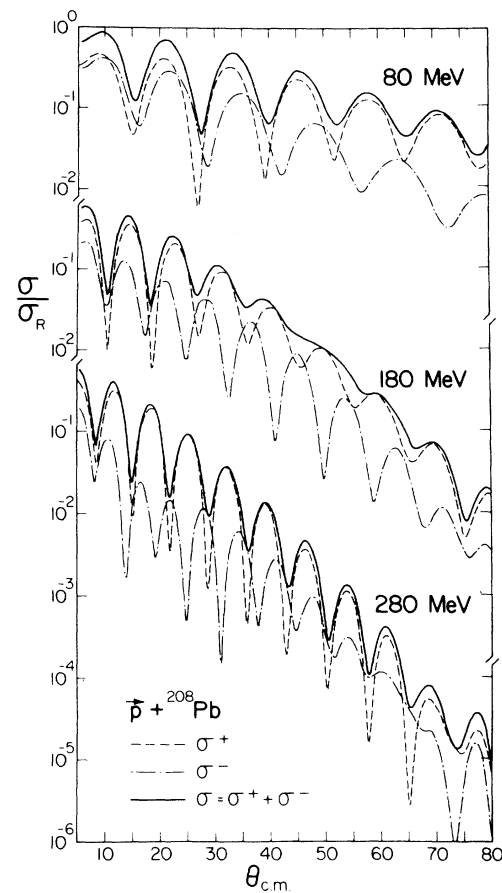


FIG. 5. Calculated differential cross section angular distributions (solid curves) plotted as ratio-to-Rutherford for 80, 180, and 280-MeV proton elastic scattering from  $^{208}\text{Pb}$ . The partial spin-channel decomposition of the cross sections ("spin up" dashed curves; "spin-down" dot-dashed curves) is also plotted, illustrating the origin of the damping of the oscillatory structure observed around 180 MeV.

splittings can be readily understood in terms of the effects of real and imaginary SO terms on the total nuclear potential. As illustrated in Fig. 6 (for  $^{90}\text{Zr}$  at 135 MeV,  $L = 10$ ) the real SO component for  $J = L + \frac{1}{2}$  effectively increases the radius of the total nuclear potential, resulting in a larger real phase shift  $\delta_L^+$ . The imaginary SO part reduces the absorption in the surface region, thus raising  $\eta_L^+$ . For  $J = L - \frac{1}{2}$  the effects are in the opposite direction. These effects of  $V_{\text{so}}$  and  $W_{\text{so}}$  on  $\delta$  and  $\eta$  are almost completely decoupled;  $V_{\text{so}}$  almost exclusively causes the splitting of  $\delta$  without affecting  $\eta$ , while  $W_{\text{so}}$  alone is responsible for the splitting of  $\eta$  without affecting  $\delta$ .

Even though the differential cross section at medium energies exhibits significant sensitivity to the SO term in the OM potential, it is clear from the substantial scatter with energy and target mass of the SO parameters obtained (see Secs. III C 1–III C 3) from fitting  $\sigma(\theta)$ , that cross section data by themselves are insufficient to define the SO potential unambiguously and with the desired precision. It is then appropriate to ask with what precision polarization measurements need to be carried out to further constrain the SO parameters. Model calculations of  $P(\theta)$  within the range of present parameter uncertainties show that in order to define  $V_{\text{so}}$  and  $W_{\text{so}}$  to better than  $\pm 0.3$  MeV, exclusive of parameter correlations,  $P(\theta)$  needs to be measured to within an average precision of about  $\pm 0.03$ . Existing  $P(\theta)$  data at medium energies are for the most part *not* sufficiently precise to define the SO potential to this degree.

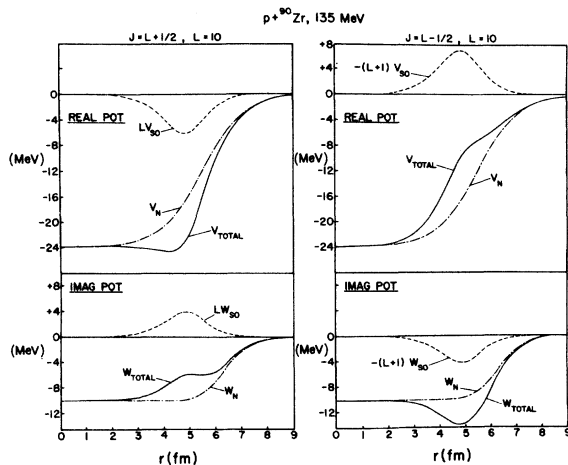


FIG. 6. Spin-orbit effects on the real and imaginary parts of the total nuclear potential for  $^{90}\text{Zr}$  at 135 MeV for the  $L = 10$  partial wave. The left-hand panel illustrates the case  $J = L + \frac{1}{2}$ , the right-hand panel the case  $J = L - \frac{1}{2}$ . In each case the dot-dashed line shows the central nuclear potential, the dashed line the spin-orbit potential, and the solid line the effective total potential.

## B. Energy and target mass dependence of the optical potential

### 1. The central potential

Because of significant correlations generally encountered among the geometry and strength parameters of the Woods-Saxon form used to characterize OM potentials, the individual parameters generally exhibit continuous ambiguities which can obscure systematic trends with energy  $E_p$  or target mass  $A$ . One therefore customarily looks for trends in the potential volume integrals and the potential rms radii. Alternatively, the use of prescribed potential form factors in constrained-geometry searches on the data will generally yield values of the potential strengths which are well behaved with  $E_p$  and  $A$ . In the present analysis both approaches were taken and the results are discussed in this section.

In Fig. 7(a) we present the central potential volume integrals for  $^{40}\text{Ca}$ ,  $^{90}\text{Zr}$ , and  $^{208}\text{Pb}$  obtained from the best-fit, fixed-geometry, and fixed-SO analyses, as a function of bombarding energy  $E_p = 40$ –180 MeV (the 40 MeV results are from a reanalysis of the data of Ref. 5). Note the logarithmic energy scale. For the *real* volume integral  $J_R/A$  (top half) no systematic target dependence is observed. The scatter in the individual values of  $J_R/A$  about an energy-dependent average value given by the straight lines is of order  $\pm 5\%$ . These fluctuations are consistent with an average uncertainty of about  $\pm 5\%$  in the fitted parameters based on an absolute normalization error of up to  $\pm 10\%$  in the cross section data. The real volume integrals clearly follow a logarithmic energy dependence of the form  $J_R/A = J_R^0/A - \beta \ln E_p$  ( $E_p$  in MeV) with  $J_R^0/A \approx 815 \pm 15$  MeV fm $^3$ ,  $\beta \approx 120$  MeV fm $^3$  for both best-fit and fixed-geometry results, and  $J_R^0/A \approx 765 \pm 10$  MeV fm $^3$ ,  $\beta \approx 110$  MeV fm $^3$  for the fixed-SO results. These energy dependences are represented by the straight lines in the upper half of Fig. 7(a). We consider the latter parametrization to be the more realistic of the two.

The present analysis yields a somewhat smaller slope parameter  $\beta$  for the energy dependence of the real central volume integral than the global analysis of  $p + ^{208}\text{Pb}$  scattering by van Oers *et al.*<sup>11</sup> which gave  $\beta = 150$  MeV fm $^3$ . That analysis relied on the Orsay data<sup>9</sup> at 156 MeV and the Uppsala data<sup>11</sup> at 185 MeV, both of which covered a limited angular range. Note that a reanalysis of the Orsay and Uppsala data within the present relativistic framework does not bring the results [shown in Fig. 7(a) by the star symbols] in line with the new results at similar energies.

The values for the *imaginary* volume integral

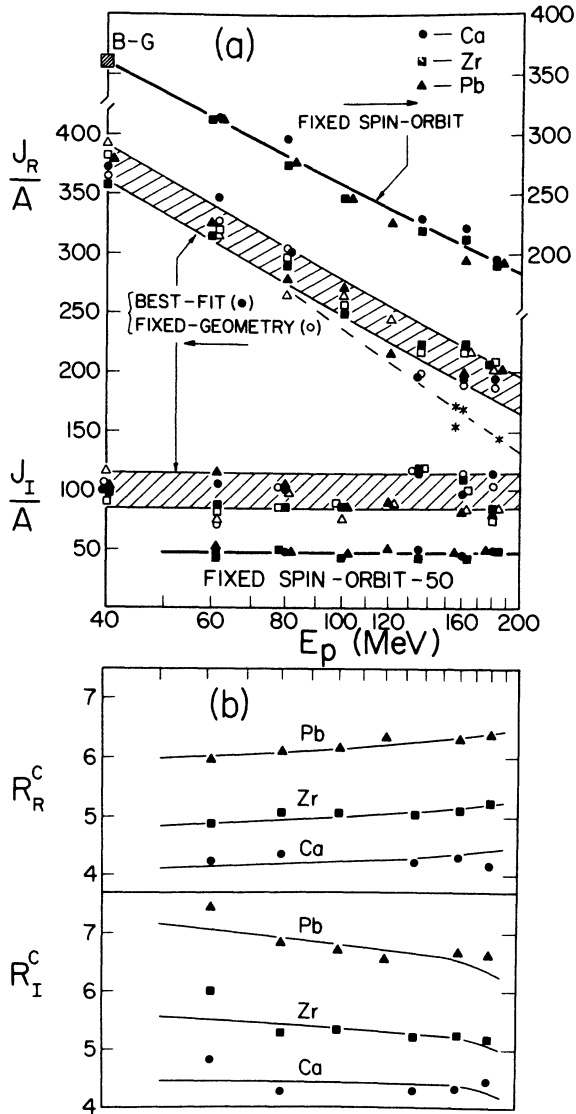


FIG. 7. (a) Normalized volume integrals  $J_R/A$ ,  $J_I/A$  of the complex central potential from the "best-fit" analysis (solid symbols), the "fixed-geometry" analysis (open symbols), and the "fixed-SO" analysis. The star symbols are based on the data of Refs. 9, 11, and 12; the 40-MeV point, labeled B-G, is the Becchetti-Greenlees result (Ref. 23) for Zr. The solid line and shaded band for  $J_R/A$  represent the average logarithmic energy dependence of the present results, the dashed line the result of the van Oers analysis (Ref. 11). The horizontal line and shaded band for  $J_I/A$  are drawn to emphasize the constancy with energy indicated by the data. (b) Root-mean-square radii  $R_R^c$ ,  $R_I^c$  of the real and imaginary central potentials as a function of proton energy. The data points represent the best-fit results, the curves are results of the fixed-SO analysis.

$J_I/A$  obtained in the best-fit and fixed-geometry analyses are seen to scatter more widely ( $\pm 20\%$ ) than those for the real potential around a mean value of about  $100 \text{ MeV fm}^3$ , as illustrated in the

lower half of Fig. 7(a). The values obtained in the fixed-SO analysis, on the other hand, are much better defined:  $J_I/A \approx 98 \pm 5 \text{ MeV fm}^3$ . This quantity does not exhibit any discernable systematic variation with  $E_p$  or  $A$ .

Extrapolation of the present results for  $J_R/A$  for  $E_p > 60$  MeV to lower energies shows a good match with results of previous lower-energy analyses, e.g., at 40 MeV the Becchetti-Greenlees (BG) global potential<sup>23</sup> gives  $J_R/A \approx 360 \text{ MeV fm}^3$ , compared to  $\sim 375$  ( $360$ )  $\text{MeV fm}^3$  for the present best-fit (fixed-SO) results. The BG value of  $\sim 80 \text{ MeV fm}^3$  for  $J_I/A$  is somewhat below our values of  $\sim 100 \text{ MeV fm}^3$  valid for  $E_p \geq 60$  MeV. However, we expect the absorption to decrease continuously with decreasing energy below 40 to 50 MeV.

While the rms radii for the central potentials obtained in the best-fit and fixed-geometry analyses (listed in Tables I and II) exhibit no systematic dependence on proton energy over the range 80–180 MeV [see Fig. 7(b)], the results of the fixed-SO analysis show a 5% increase in  $R_R^c$  and slight (or no) decrease in  $R_I^c$  over this energy range. The fixed-SO results for  $R_R^c$  and  $R_I^c$  in the middle of this range ( $E_p \sim 130$  MeV) are in very good agreement with the energy-averaged best-fit values. At the lower end of the energy range,  $R_I^c$  is nearly the same as  $R_R^c$  for  $^{40}\text{Ca}$ , slightly larger than  $R_R^c$  for  $^{90}\text{Zr}$ , and substantially larger than  $R_R^c$  for  $^{208}\text{Pb}$ . Near 180 MeV, on the other hand, we find  $R_I^c \approx R_R^c$ , consistent with the observation  $r_w - r_0$  and  $a_w - a_0$  as  $E_p \rightarrow 200$  MeV. The energy-averaged values of the rms radii closely follow the  $A^{1/3}$  dependence on target mass also found in low-energy analyses; here  $R_R^c \approx 1.6 + 0.78A^{1/3}$  and  $R_I^c \approx 1.0 + 0.96A^{1/3}$ .

The real central potential strength  $V$  obtained in the fixed-SO analysis and displayed as a function of  $E_p$  in Fig. 4, exhibits a clear dependence on both  $A$  and  $E_p$ . The energy dependence of  $V$  is qualitatively similar to that of the volume integral  $J_R/A$ , namely a linear dependence on  $\ln E_p$ , and the variation of  $V$  with target mass  $A$  is consistent with a linear dependence on relative neutron excess  $(N - Z)/A$ . These results for  $V$  can thus be parametrized (with  $E_p$  in MeV) as

$$V \text{ (MeV)} = \left( 92.5 + 64 \frac{N - Z}{A} \right) (1 - 0.155 \ln E_p) \quad (9)$$

over the energy range  $E_p \approx 60$ –180 MeV. Individual values generally fluctuate about this average behavior by less than  $\pm 0.7$  MeV.

The isospin-dependent potential  $V$  is conventionally written as a sum of isoscalar and Coulomb-corrected isovector terms, i.e.,

$$V(E_p, A, Z) = V_0(E_p) + \beta \bar{V}_c + V_1(E_p) \frac{N - Z}{A}, \quad (10)$$

where  $\bar{V}_c \approx 1.38 ZA^{-1/3}$  (MeV) and  $\beta \equiv \partial V_0 / \partial E_p \approx 0.3$  at low energies.<sup>1</sup> In the medium energy range considered here, the average slope parameter is roughly half the low-energy value. Taking  $\beta = 0.15$ , we can express the result of Eq. (9) as

$$V = 91.5 (1 - 0.157 \ln E_p) + 0.2 \frac{Z}{A^{1/3}} + V_1(E_p) \frac{N - Z}{A} \quad (11a)$$

with the isovector strength

$$V_1 = 59 (1 - 0.18 \ln E_p). \quad (11b)$$

This result for  $V_1$  for  $E_p = 60$ – $180$  is compared in Fig. 8 with lower-energy results established by previous analyses of data over a wide range of targets. It is difficult to assess the significance of our result because of the very approximate treatment of the Coulomb correction and the sensitive dependence of the extracted values for  $V_1$  on the choice of this correction term.

The values of the imaginary potential strength  $W_s$  are seen in Fig. 4 to remain relatively constant between 80 and 160 MeV;  $W_s \sim 7.0$  MeV for  $^{40}\text{Ca}$  to  $W_s \sim 8.5$  MeV for  $^{208}\text{Pb}$ . These rather shallow absorptive potentials are characterized by a relatively large radial extent, with effective radii of  $(1.40$ – $1.45) A^{1/3}$  as compared to  $(1.21$ – $1.26) A^{1/3}$  for the real central potential. Beyond 160 MeV,  $W_s$  increases and  $r_w$  decreases. This trend continues and accelerates beyond 200 MeV (Ref. 24) as major new absorption channels (e.g., pion production) become significant and the largely peripheral low-energy absorption mechanisms

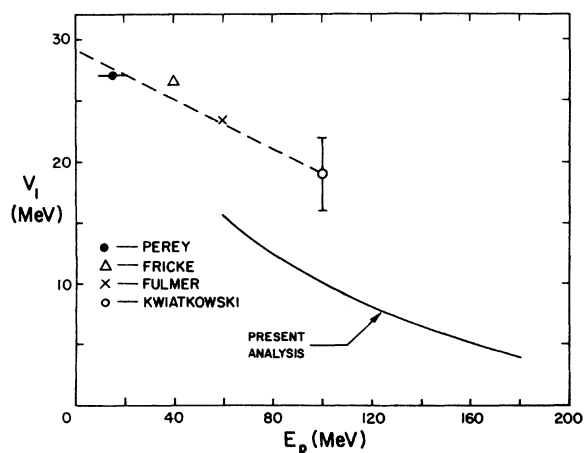


FIG. 8. Strength of the real isovector (symmetry) potential obtained in the present analysis of proton scattering between 80 and 180 MeV (solid curve), using a conventional empirical prescription for the Coulomb correction, together with results from previous work<sup>1,6-8</sup> (data points and dashed curve).

give way to quasifree two-nucleon effects proportional to the nucleon density.

## 2. The spin-orbit potential

The normalized volume integrals of the real and imaginary spin-orbit potentials are shown in Fig. 9. The solid and shaded symbols are the best-fit results, the open symbols the fixed-geometry results. The values obtained from fitting cross sections alone are shown by small symbols, those from simultaneous analyses of cross-section and polarization data<sup>8,11,12,19,20,26</sup> are depicted by the large symbols. Although the results of cross section analyses show a large amount of scatter, an overall trend with  $E_p$  is discernable, i.e.,  $K_R^{so}$  decreases with increasing  $E_p$ , while  $K_I^{so}$  appears to be largely energy independent. A much better defined systematic energy dependence is indicated for both  $K_R^{so}$  and  $K_I^{so}$  by the recent, precise 65-MeV and 135-MeV  $^{90}\text{Zr}$  analyzing power measurements and the older 160 MeV and 180 MeV  $^{40}\text{Ca}$  polariza-

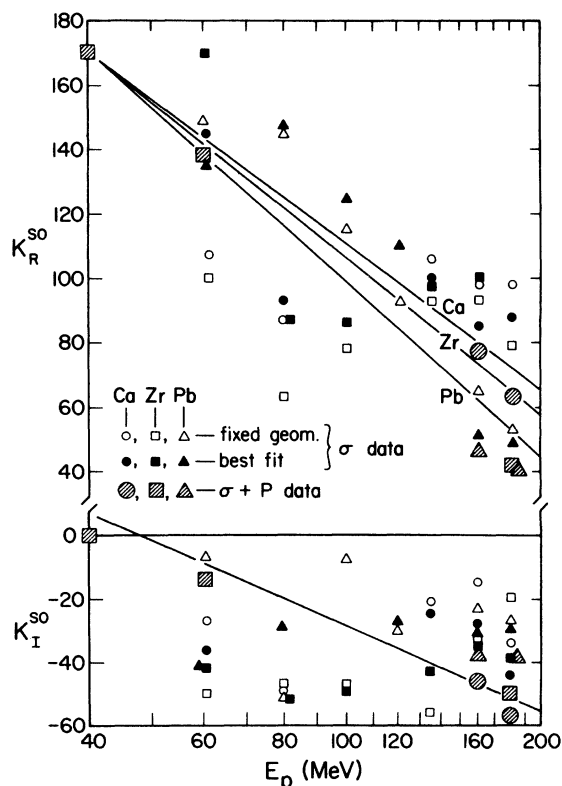


FIG. 9. Empirical values (points) of the normalized volume integrals,  $K_R^{so}$  and  $K_I^{so}$ , of the spin-orbit potential together with the average trend (lines) based on the preliminary analyzing power analysis of Ref. 21. The small solid (open) symbols represent best-fit (fixed-geometry) analyses of cross sections only, while the large symbols show the results of fitting cross-section and polarization data simultaneously.

tion data. The trends of these results are in fact well represented by the solid lines in Fig. 9 which illustrate the behavior deduced from the recent, preliminary analyses of new analyzing power data<sup>21</sup> which formed the basis of the present fixed-SO analysis. The real and imaginary SO strength parameters  $V_{so}$  and  $W_{so}$ , deduced from Eqs. (7a)–(7c), can be represented for  $E_p \geq 40$  MeV as

$$V_{so}(E_p) \approx 16.5 - (2.75 \pm 0.10) \ln E_p, \quad (12a)$$

$$W_{so}(E_p) \approx 5.2 - 1.36 \ln E_p, \quad (12b)$$

("+" for <sup>208</sup>Pb, and "-" for <sup>40</sup>Ca in Eq. (12a), all parameters  $V_{so}$ ,  $W_{so}$ , and  $E_p$  in MeV). The real SO strength parameter (or volume integral) decreases substantially with increasing energy, while the imaginary SO strength parameter (or volume integral) is seen to be of opposite sign and increases with energy, approaching in magnitude that of the real SO strength near 200 MeV.

The falloff of  $V_{so}$  with energy is essentially identical with that of the real central strength  $V$  (ignoring any isospin dependence), i.e.,  $V_{so}(E_p) \approx 0.16 V(E_p)$ . The commonly assumed proportionality between  $V_{so}$  and  $V$  at very low energies<sup>27</sup> thus appears to persist at much higher energies. While  $W_{so}$  shows no significant dependence on  $A$  or  $(N - Z)$ , a pronounced target dependence becomes evident in  $V_{so}$  at high energies. The behavior we find at lower energies is consistent with the results of a recent reanalysis of the spin-orbit term in the nucleon optical potential for bound state as well as scattering energies.<sup>28</sup>

In connection with the pronounced energy dependence of the real SO strength parameter  $V_{so}$ , Eq. (12a), it is worthwhile to recall that, in contrast to the real central potential strength  $V(E_p)$ ,  $V_{so}(E_p)$  does *not* represent the actual effective real spin-orbit strength and its energy dependence. Rather, the peak value of the real SO potential (here denoted by  $\hat{U}_{so}$ ) is attained at the nuclear surface,  $r = R_{so}$ , for which  $\hat{U}_{so} = V_{so}/(2R_{so}a_{so})$ . The actual strength experienced by the surface partial waves, characterized by  $L_{\text{eff}} = kR_{so}$ , is then given by  $\hat{U}_{so} \times \langle \vec{L}_{\text{eff}} \cdot \vec{\sigma} \rangle \approx \pm k(V_{so}/2a_{so})$  since  $J_{\text{eff}} \approx L_{\text{eff}}$  for  $L_{\text{eff}}$  large (of order 10–20 in this energy region). The variation of this effective SO strength with energy is in fact found to be quite weak because the explicit velocity dependence of the  $\vec{L} \cdot \vec{\sigma}$  operator effectively cancels the energy dependence exhibited by the SO peak strength  $\hat{U}_{so}$  through  $V_{so}(E_p)$ . The interesting implication of this result is the relatively stronger influence that the SO interaction should assume with increasing energy; while the effective SO potential remains essentially constant, the central potential decreases with energy, thus enhancing the importance of SO effects as the

energy approaches 200 MeV.

The pronounced energy dependence observed for  $V_{so}$  (and hence for  $\hat{U}_{so}$ ) is somewhat surprising since it is in disagreement with most theoretical predictions (see the following section); we would expect any energy dependence arising from non-locality to be less for the equivalent local SO term than for the equivalent local central term because of the shorter range of the two-nucleon SO force.

### C. Comparison with theory

Microscopic calculations of the optical potential in terms of a realistic (i.e., strong) nucleon-nucleon interaction  $v$  are based on Brueckner-Hartree-Fock (BHF) or multiple-scattering expansions. The BHF approximation yields a non-local and intrinsically energy-dependent OM potential. The most recent and thorough developments of this parameter-free model, thought to be valid up to about 200 MeV, are due to Jeukenne, Lejeune, and Mahaux<sup>30</sup> (JLM) and Brieva and Rook<sup>29</sup> (BR). Of the two formulations, only the BR calculation incorporates the complex SO potential. These authors use an effective, complex transition matrix  $t = v + vGt$  and a generalized reference spectrum method to solve the Bethe-Goldstone equation. For comparison with the phenomenological OM, a complex and energy-dependent local potential is generated with the antisymmetrized folding model and the local density approximation. Reasonably good fits to experimental data have been obtained with this model at energies below 100 MeV.

At energies beyond 200 MeV, multiple-scattering theory in the impulse approximation (IA), in which the reaction matrix reduces to the transition matrix for free nucleon-nucleon scattering, is expected to provide a simple and useful description. Recent application of this model in the KMT approach<sup>31</sup> to medium-energy (100–200 MeV) proton-nucleus scattering by Schwandt and Petrovich<sup>32</sup> has been modestly successful. These calculations were carried out to lowest order using the Love parametrization<sup>33</sup> of the complex  $t$  matrix, antisymmetrized to incorporate the effect of knockon exchange.

We choose here to make the comparison between phenomenology and theory in terms of the respective potential volume integrals and rms radii. In Fig. 10 our empirical results for  $J_R/A$  are shown along with the microscopic model results of BR, JLM, and the IA. The IA results for  $J_R/A$  are too high by about 10% around 100 MeV but agree well with the phenomenological results near 200 MeV. The rapid falloff of the BR and JLM results with  $E_p$  above about 80 MeV results

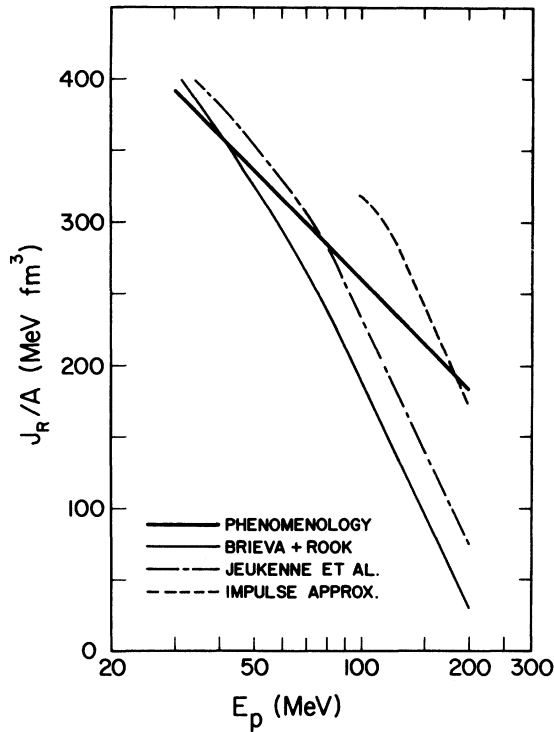


FIG. 10. Comparison of the phenomenological results for the real central volume integral with predictions of various microscopic formulations of the OM potential (Refs. 29, 30 and 32).

from the increasing deviation of the real central form factor from a Woods-Saxon shape. The theoretical potentials beyond  $E_p = 100$  MeV are characterized by a pronounced dip in attraction just inside the nuclear surface resulting from cancellation between two large components of the potential: the *direct* (local) part which is repulsive, largely independent of  $E_p$ , and of order  $+100$  MeV in the nuclear interior, and the *exchange* part (of nonlocal origin) which is attractive and decreases with increasing  $E_p$  from typically  $-150$  MeV at very low  $E_p$  to about  $-100$  MeV for  $E_p$  near 200 MeV. The approach used by BR for transforming to an equivalent *local* potential, however, becomes inadequate at the higher energies. This has been demonstrated recently by von Geramb<sup>40</sup> who solved the nonlocal Schrödinger equation with the BR nonlocal potential exactly and (in terms of this solution) defined a “phase equivalent” local potential which bears much greater resemblance to the phenomenological potential above 100 MeV than the “trivially” equivalent local potential of BR.

The empirical values found here for the imaginary central volume integral  $J_I/A$  ( $90$ – $105$  MeV  $\text{fm}^3$ ) agree well with the calculations of BR ( $80$ – $105$  MeV  $\text{fm}^3$ ) in the energy region  $40$ – $100$  MeV, while

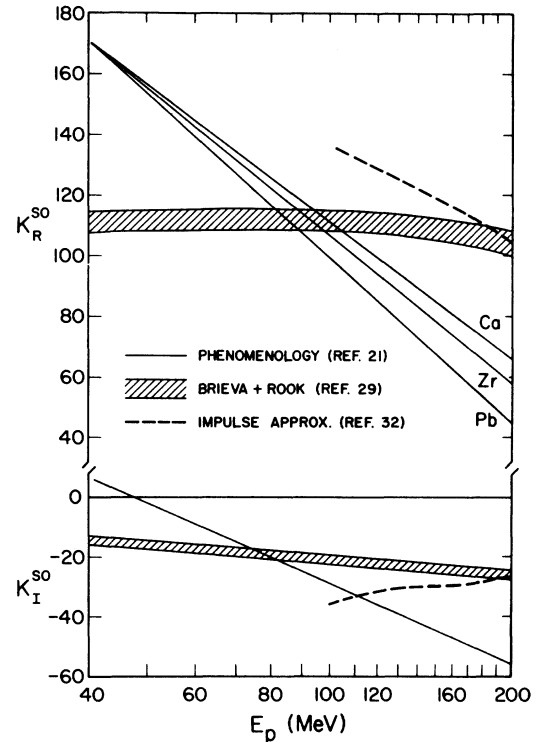


FIG. 11. Comparison of the phenomenological results for the real and imaginary spin-orbit potential volume integrals with predictions of two microscopic formulations of the OM potential.

the theoretical values of JLM are universally too large (of order  $120$ – $140$  MeV  $\text{fm}^3$ ). This may be because the JLM calculations apply to the average “nuclear-matter” nucleus, while for the nuclei studied here, the density of nuclear states is much less and fewer reaction channels are available. The IA values for  $J_I/A$  are too large by about a factor of 2 at all energies. Corrections to the first-order IA for sizable Pauli blocking effects are expected to improve these results considerably.

The rms radii of the central potentials, both real and imaginary, calculated by BR for  $^{40}\text{Ca}$  and  $^{208}\text{Pb}$  above 40 MeV, agree well with our results in magnitude and overall energy dependence (i.e.;  $\partial R_R^c/\partial E_p > 0$ ,  $\partial R_I^c/\partial E_p < 0$ ). In contrast, the predictions of JLM are systematically too small at the higher energies ( $> 100$  MeV), by  $\sim 5\%$  for  $R_R^c$  and by  $\sim 20\%$  for  $R_I^c$ , indicating that the local density approximation used to construct the OM potential for finite nuclei is not accurate in the surface region.

The results of BR calculations for the real and imaginary SO volume integrals  $K_{R,I}^{\text{so}}$  are presented in Fig. 11 for comparison with phenomenological results; the width of the shaded region indicates the calculated variation with target mass. The

failure of the BR calculations to reproduce the strong empirical energy dependence is evident. These calculations underestimate the real part  $K_R^{so}$  below  $\sim 80$  MeV and overestimate it above  $\sim 120$  MeV; the predicted imaginary part  $K_I^{so}$  appears to be considerably too small at the higher energies where our choice of *identical* radial form factors for  $V_{so}$  and  $W_{so}$  in fact conforms to the theoretical expectation (the BR calculations show this assumption to be poor below  $\sim 100$  MeV). Results for the impulse approximation are seen to approach the BR calculations above 160 MeV. The IA predicts the empirical falloff of  $K_R^{so}$  with energy but is too large in magnitude. The IA result for  $K_I^{so}$  shows little energy dependence and is somewhat too small at higher energies. It is, again, likely that Pauli blocking corrections to the first-order IA calculations, expected to be sizeable at energies below 200 MeV, will bring the IA results into closer agreement with the phenomenological results.

### 1. Reaction cross section and mean free path

The reaction cross sections calculated from the optical potentials obtained in the various phases of analysis are illustrated as a function of energy in Fig. 12 together with published experimental

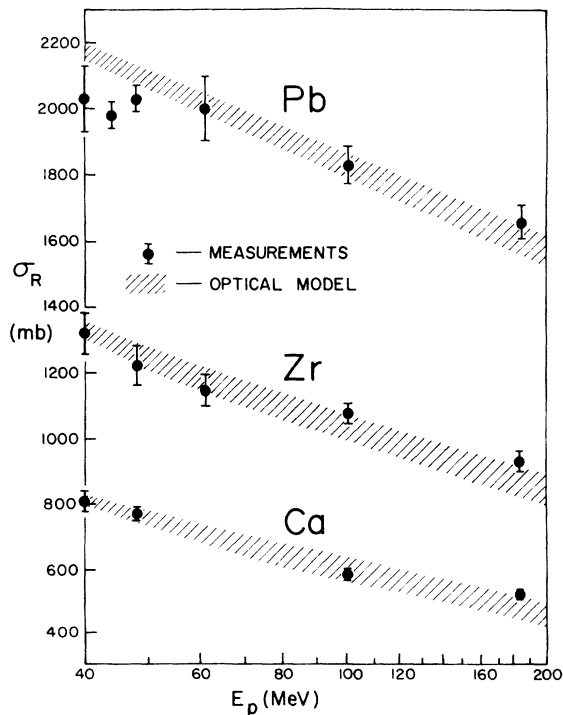


FIG. 12. Comparison of the OM results for the reaction cross section with measured values (Ref. 34). The shaded bands indicate the range of OM values for  $\sigma_R$  obtained in the various phases of analysis and listed in Tables I-III.

data.<sup>34</sup> The shaded bands in Fig. 12 indicate the range of the optical-model values at each energy. The overall agreement with measurements is seen to be reasonably good except for Pb at the lowest energies.

Semiclassically the absorption of a proton of energy  $E$  by a nucleus is viewed as the attenuation of the nucleon plane wave traversing a complex spherical square well of effective radius  $R = R_n + \lambda$ , where  $R_n$  is the nuclear absorption radius and  $\lambda$  the reduced deBroglie wavelength of the incident proton. The reaction cross section is related to the absorption coefficient  $K$  (the reciprocal of the nucleon mean free path  $\lambda_m$ ) in nuclear matter as<sup>35</sup>

$$\sigma_R = \pi R^2 (1 - V_c/E)(1 - T), \quad (13)$$

where the factor  $(1 - V_c/E)$  allows for Coulomb repulsion in the compound-nucleus formation ( $V_c \equiv Ze^2/R_n$ ), and  $T$  is the transparency of the nucleus defined as

$$T = \frac{1 - (1 + 2KR)e^{-2KR}}{2K^2R^2}. \quad (14)$$

The nuclear mean free path (mfp)  $\lambda_m$  and transparency  $T$  were calculated for  $^{40}\text{Ca}$ ,  $^{90}\text{Zr}$ , and  $^{208}\text{Pb}$  in the energy range 40-180 MeV from the optical-model values of  $\sigma_R$ . In these calculations  $R_n$  was taken to be  $(2.15 - 0.16 \ln E_p)A^{1/3}$  fm, a relation which represents the trend of values used in earlier fits to  $\sigma_R$  data for many targets over a wide range of energies.<sup>34</sup> These values of  $R_n$  are also close to the values obtained in the present analysis for the radius of the imaginary central potential in the 100-180 MeV range of proton energies. The results for  $T$  and  $\lambda_m$  are presented as a function of energy in Fig. 13. The shaded bands are based on the range of  $\sigma_R$  values (shown in Fig. 12) which are given by the various optical potentials derived in this analysis. Both the nuclear transparency and the proton mfp are seen to increase with energy, reaching a maximum around 200 MeV (beyond 250 MeV,  $T$  and  $\lambda_m$  decrease again due to the increasing pion production cross section).<sup>36</sup> The mfp is essentially similar for all nuclei. The transparency decreases appreciably with nuclear size simply because the mfp becomes a smaller fraction of the nuclear diameter. Over the energy range of the present work, 80-180 MeV,  $\lambda_m$  increases only mildly with energy and lies within the range  $5.2 \pm 1$  fm. Using the well-known semiclassical relation for  $\lambda_m$  in terms of the imaginary part  $W$  of the optical square-well potential and the effective projectile velocity  $v$  inside the nuclear well,  $\lambda_m = \hbar v / 2W$ , one obtains  $W \approx 10$  MeV around  $E_p \approx 150$  MeV. The associated radius is  $R_n = 1.35A^{1/3}$  fm. These values are in reasonable agreement with the ac-

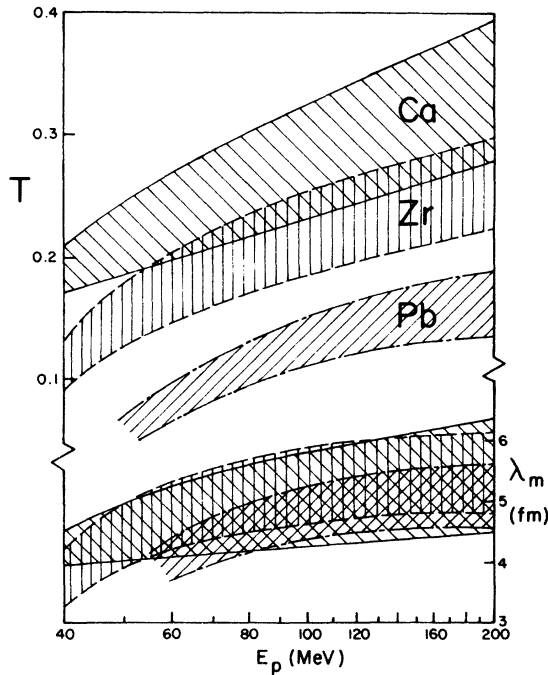


FIG. 13. Nuclear transparency  $T$  and mean free path  $\lambda_m$  for protons in nuclei for proton energies between 40 and 200 MeV. The shaded bands indicate the range of values calculated from OM reaction cross sections (as displayed in Fig. 12).

tual values  $W \approx 8-9$  MeV,  $R_w \approx 1.37A^{1/3}$  fm found for heavy nuclei such as  $^{90}\text{Zr}$  or  $^{208}\text{Pb}$  in the optical model analysis of the differential cross section data. Application of the semiclassical model at these energies thus seems to be a reasonable approach to the problem of extracting semiquantitative information about nuclear transparency from the scattering data. The specific values obtained here for  $\lambda_m$ , of course, depend sensitively on the choice of absorption radius  $R_n$ , e.g., a 3% decrease in  $R_n$  typically corresponds to a 20% reduction in  $\lambda_m$ . A reasonable estimate of the uncertainty in  $R_n$  of  $\pm 0.04A^{1/3}$  within the energy range of interest thus contributes about  $\pm 1$  fm to the error in  $\lambda_m$ .

The mfp for a proton traversing nuclear matter may also be related to the effective, isospin-averaged cross section  $\hat{\sigma}$  for a nucleon-nucleon collision inside nuclear matter of density  $\rho$ , through the expression  $1/\lambda_m = \rho\hat{\sigma}$ . In terms of the total cross section  $\sigma$  for *free* nucleon-nucleon scattering, we can express  $\hat{\sigma}$  as  $\hat{\sigma} = \sigma(E)P(E_F/E)$ , where  $E(E_F)$  is the incident (Fermi) energy and  $P$  is the so-called Pauli blocking factor. The Fermi-gas model estimate of this factor is<sup>37</sup>  $P(X) = 1 - (7/5)X$ , where  $X \equiv E_F/E$ . Near 200 MeV,  $P(X) \approx 0.75$  (using  $E_F = 40$  MeV),  $\sigma_{pp} = 2.4$  fm<sup>2</sup>, and  $\sigma_{pn} = 4.2$  fm<sup>2</sup>. The standard value of  $\rho = 0.16$  fm<sup>-3</sup>

then yields  $\lambda_m \approx 2.5$  fm, or about half of the empirical value obtained from the proton-nucleus reaction cross section  $\sigma_R$ . However, it should be kept in mind that, in the simple transmission picture of a nucleon traversing nuclear matter, a nucleon-nucleon collision does not necessarily lead to a nuclear reaction, and that therefore the collision mean free path calculated from  $\hat{\sigma}$  may indeed be shorter than the reaction mfp which is related to the reaction cross section  $\sigma_R$ .

## 2. Total cross section and forward scattering amplitude

We have also calculated the total cross section  $\sigma_T \equiv \sigma_R + \sigma_{\text{elastic}}$  for proton-nucleus scattering from optical potentials, as well as the ratio  $\alpha \equiv \text{Re}f_N(0^\circ)/\text{Im}f_N(0^\circ)$ . Here  $f_N(0^\circ)$  is the spin-independent nuclear forward-scattering amplitude *without* the Coulomb phases and is given by

$$f_N(0^\circ) \equiv \frac{1}{k} \sum_L [(L+1)\gamma_L^+ + L\gamma_L^-], \quad (15)$$

where  $\gamma_L^\pm \equiv (1/2i)(S_L^\pm - 1)$  in terms of the scattering matrix elements  $S_L^{J=L \pm 1/2}$  which in turn are calculated from the optical potential *including* the Coulomb term. The optical theorem relates  $\sigma_T$  and  $\text{Im}f_N(0^\circ)$  by  $\sigma_T = (4\pi/k)\text{Im}f_N(0^\circ)$ . Beyond about 180 MeV, measurements of proton total cross sections and values of  $\alpha$  for elements with  $A \leq 16$  have recently been published.<sup>38</sup> The purpose of our OM calculation of these quantities for the wider range of nuclei  $^{12}\text{C}$ ,  $^{28}\text{Si}$ ,  $^{40}\text{Ca}$ ,  $^{90}\text{Zr}$ , and  $^{208}\text{Pb}$  was two-fold: (a) to compare the OM results obtained over the energy range 80–180 MeV to higher-energy measurements, and (b) to relate our results to the data for free-proton-nucleon scattering as a further check on the applicability of the impulse-approximation treatment of proton-nucleus scattering below 200 MeV. Also, as pointed out by Schwaller *et al.*,<sup>38</sup> the ratio  $\alpha$  can provide a valuable constraint on optical-model analyses of data because it is sensitive to the absolute values of the cross section at small angles.

Our results for  $\alpha$  and the total cross section per target nucleon  $\sigma_T/A$  are presented graphically in Fig. 14 together with the trend of experimental proton-nucleus data of Schwaller *et al.*<sup>38</sup> (shaded areas). The solid curve in the upper panel represents the isospin-averaged nucleon-nucleon ( $NN$ ) total cross section  $\sigma_T(NN) \equiv \frac{1}{2}(\sigma_{pp} + \sigma_{pn})$ ; the solid curve in the lower panel is the value of  $\alpha$  for  $NN$  scattering  $\alpha_{NN}$  in terms of the isospin-averaged  $NN$  amplitude  $f_{NN} = \frac{1}{2}(f_{pp} + f_{pn})$  due to Grein.<sup>39</sup> We see that the optical-model results for  $\sigma_T/A$  and  $\alpha$  for the lighter nuclei ( $A \leq 90$ ) at 200 MeV match well with the high-energy measurements. Below 200 MeV,  $\sigma_T/A$  exhibits strong residual target-

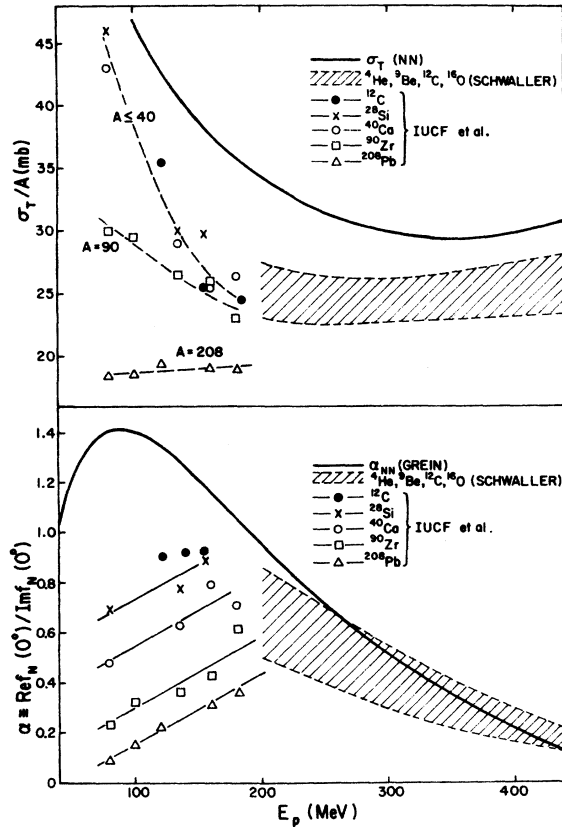


FIG. 14. Total cross section per target nucleon  $\sigma_T/A$  (top panel) and the ratio  $\alpha$  of real to imaginary parts of the spin-independent forward scattering amplitude (bottom panel) for proton scattering from various targets as a function of bombarding energy. The solid lines represent isospin-averaged values of  $\sigma_T$  and  $\alpha$  for free proton-nucleon scattering.

mass dependence for  $A > 40$ . For proton-nucleus scattering  $\sigma_T/A$  is consistently smaller by 15–50% than  $\sigma_T(NN)$  between 100 and 400 MeV. For heavier nuclei, however,  $\sigma_T/A$  turns out to be remarkably close to the value for  $\sigma_T(NN)$  after correcting the latter quantity for Pauli blocking using Fermi gas model estimates (see preceding section). The ratio  $\alpha$  below 200 MeV varies appreciably with both  $A$  and  $E$  and is also significantly smaller than  $\alpha_{NN}$ . For the lighter targets ( $A \leq 40$ ), however,  $\alpha$  approaches  $\alpha_{NN}$  near 200 MeV. For an isospin-zero target, the proton-nucleus forward amplitude  $f$  is related to the isospin-averaged  $NN$  amplitude  $f_{NN}$  in the impulse-approximation model by  $f = A f_{NN}$ . Thus, in that model the ratio  $\alpha$  is independent of  $A$  and equal to  $\alpha_{NN}$ .

## V. SUMMARY AND CONCLUSION

Eleven cross-section angular distributions for proton elastic scattering from  $^{40}\text{Ca}$ ,  $^{90}\text{Zr}$ , and

$^{208}\text{Pb}$  targets were measured at several energies between 80 and 180 MeV. The new measurements cover about twice the angular range of previous data in this energy range and were made in sufficiently small angular steps to define accurately the structure of the angular distributions. The precision of the data is quite good, with relative and systematic errors generally below 3% and 10%, respectively. The most striking general feature of the angular distributions is the disappearance of characteristic diffractive oscillations at intermediate angles at energies beyond 100 MeV. This damping was found to be a manifestation of the spin dependence in the proton-nucleus interaction potential which is effectively much stronger (relative to the central potential) at these energies than below 60 MeV.

The data obtained in this work, along with the recent 100-MeV Maryland data, serve adequately to establish the systematic features of elastic proton scattering between 60 MeV and 180 MeV. The present analysis of the extensive new cross-section data has resulted in a greatly improved knowledge of the medium-energy optical potentials; the lack of sufficient data in the energy region between 60 and 180 MeV has previously hampered reliable definition of the phenomenological optical-model potential and its systematic dependence on energy. The new data also provide discriminating tests of the validity of various microscopic formulations of the optical-model potential and its energy dependence.

The present data are very well described by an optical potential with Woods-Saxon form factors, but are effective in reliably defining the parameters of even the central components of the optical potential only for a realistically constrained spin-orbit parametrization. The parametrization of the spin-orbit potential, although better defined by the cross sections than anticipated, still exhibits appreciable ambiguities and uncertainties. Use of existing polarization data in the analysis did not generally improve this situation very much because of the low quality of most of the polarization data. The addition of new polarization data of high quality now becoming available at energies between 80 and 180 MeV will undoubtedly refine the spin dependence of the model considerably; initial results from a partial analysis of this new data were in fact used in the present analysis to constrain the parameters of the spin-orbit potential. In such a constrained search on the cross section data the average dependence of the optical potential parameters on bombarding energy  $E_p$  (in MeV) and target mass  $A$  (in amu) was found to be represented adequately by the relations, valid for  $80 \leq E_p \leq 180$  MeV,

$$\begin{aligned}
 V &\simeq \left(92.5 + 64 \frac{N-Z}{A}\right) (1 - 0.155 \ln E_p), \\
 r_o &\simeq 1.18 + (0.34 + 6.5 A^{-1}) 10^{-3} E_p, \\
 a_o &\simeq 0.77 - 1.2 \times 10^{-4} A^{0.4} (180 - E_p),
 \end{aligned} \tag{16a}$$

$$\begin{aligned}
 W_s &\simeq 3.8 + 3 \frac{N}{Z} + 1.23 \times 10^{-3} (E_p^2 - 135)^2, \\
 r_w &\simeq 1.16 + \beta \ln(185 - E_p), \quad \beta \equiv \begin{cases} 0.065, & \text{Ca} \\ 0.053, & \text{Zr} \\ 0.058, & \text{Pb} \end{cases} \tag{16b} \\
 a_w &\simeq 0.37 + 1.8 \times 10^{-3} E_p,
 \end{aligned}$$

$$\begin{aligned}
 V_{so} &\simeq 16.5(1 - \eta \ln E_p), \quad \eta = 0.160 + 0.06 \frac{N-Z}{A}, \\
 W_{so} &\simeq 5.2(1 - 0.262 \ln E_p), \\
 r_{so} &\simeq 1.015 + 5 \times 10^{-4} A, \\
 a_{so} &\simeq 0.60,
 \end{aligned} \tag{16c}$$

where all strength parameters and energies are in MeV, geometry parameters in fm, and  $E_p^2 - E_0$  implies a nonzero term only for  $E_p > E_0$ .

The unexpectedly strong energy dependence of the geometry parameters conceivably is a consequence of constraining the central potential shape to be of Woods-Saxon form at all energies. Recent microscopic derivations of the nucleon-nucleus optical potential in a Dirac-Hartree model,<sup>41,42</sup> using one-boson exchange forces between interacting nucleons, produce real central potentials which exhibit roughly WS shapes at low energies but gradually develop a pronounced depression in the nuclear interior as the bombarding energy is raised towards 200 MeV. A preliminary calculation<sup>42</sup> for the case of  $\bar{p} + {}^{40}\text{Ca}$  at 180 MeV demonstrated that such non-WS potentials can provide essentially as good a description of the  $\sigma(\theta)$  and  $P(\theta)$  data as the present analysis in terms of WS form factors, at least for momentum transfers up to  $3.5 \text{ fm}^{-1}$ . The uniqueness of the presently determined optical potentials is therefore in doubt for energies approaching 200 MeV.

The present OM analysis (with Woods-Saxon form factors and constrained SO parametrization) of the Ca, Zr, and Pb data between 40 and 180 MeV yields values for the volume integrals  $J_R, J_I$  of the real and imaginary parts of the central potential which are defined by the data to within  $\pm 5\%$ , on the average, and exhibit simple dependences on proton energy  $E_p$ . Over the energy range considered here, the variation of  $J_R$  with  $E_p$  is found

to be logarithmic ( $\partial J_R / \partial \ln E_p = \text{const}$ ), while  $J_I$  is essentially independent of  $E_p$  ( $\partial J_I / \partial E_p \simeq 0$ ). Continuation of the specific energy dependence for  $J_R$  or  $V$  found here to higher energies would imply that the real central potential becomes repulsive beyond about 600 MeV; analysis of existing data at 800 and 1050 MeV indicate<sup>24</sup> that the zero crossing of  $V$  indeed occurs near this energy.

The strength parameter  $V_{so}$  of the real spin-orbit potential was found to have essentially the same dependence on energy as the strength parameter  $V$  of the real central potential, i.e.,  $V_{so}/V \simeq \frac{1}{8}$ , independent of  $E_p$ . This behavior implies that for those surface partial waves which are most affected by the surface-peaked spin-orbit interaction, the effectiveness of the spin-orbit potential relative to the central potential increases with energy roughly as  $\sqrt{E_p}$ .

The pronounced dependence of the real central potential strength on neutron excess  $N - Z$  observed in the present analysis implies a strength of order 5–10 MeV for the isovector term, which is considerably smaller than the values of 20–25 MeV generally applied at lower energies. The magnitude and energy dependence found here, however, are not well determined because of uncertainties in the treatment of the Coulomb correction.

The reaction cross sections  $\sigma_R$  predicted by the optical potentials which fit the angular distributions are in good agreement with measured values. Over the energy region considered here,  $\sigma_R$  decreases smoothly and approximately linearly with increasing  $\ln E_p$ . This behavior of  $\sigma_R$  implies an increased nuclear transparency and larger proton mean free path  $\lambda_m$  near 200 MeV proton energy. The values obtained here,  $\lambda_m \simeq 5.2 \pm 1 \text{ fm}$  in the 100–200 MeV range, are significantly larger than those customarily quoted in the literature.

For heavier nuclei, the total cross section per nucleon, related to the imaginary part of the nuclear forward scattering amplitude, is in reasonable agreement with the effective two-nucleon ( $NN$ ) total cross section in nuclear matter, when the latter is corrected for Pauli blocking effects. This is taken to indicate the beyond 100–150 MeV, a microscopic description of the proton-nucleus interaction in terms of the free  $NN$  interaction in a first-order, Pauli-corrected impulse-approximation model may be a valid approach. Indeed, preliminary IA analyses of the present data beyond 100 MeV appear to confirm this expectation.

This work was supported in part by the National Science Foundation.

- \*Present address: University of Maryland, Cyclotron Laboratory, College Park, Maryland 20742.
- †Present address: University of Illinois, Department of Physics, Urbana, Illinois 61801.
- <sup>1</sup>F. G. Perey, Phys. Rev. 131, 745 (1963).
- <sup>2</sup>L. Rosen, J. G. Beery, A. S. Goldhaber, and E. H. Auerbach, Ann. Phys. (N.Y.), 34, 96 (1965).
- <sup>3</sup>B. W. Ridley and J. R. Turner, Nucl. Phys. 58, 497 (1964).
- <sup>4</sup>D. L. Watson *et al.*, Nucl. Phys. A92, 193 (1967).
- <sup>5</sup>L. N. Blumberg *et al.*, Phys. Rev. 147, 812 (1966).
- <sup>6</sup>M. P. Fricke, E. E. Gross, B. J. Morton, and A. Zucker, Phys. Rev. 156, 1207 (1967).
- <sup>7</sup>C. B. Fulmer, J. B. Ball, A. Scott, and L. Whiten, Phys. Rev. 181, 1565 (1969).
- <sup>8</sup>K. Kwiatkowski and N. S. Wall, Nucl. Phys. A301, 349 (1978).
- <sup>9</sup>V. Comparat *et al.*, Nucl. Phys. A221, 403 (1974).
- <sup>10</sup>P. G. Roos and N. S. Wall, Phys. Rev. 140, B1237 (1965).
- <sup>11</sup>W. T. H. van Oers *et al.*, Phys. Rev. C 10, 307 (1974).
- <sup>12</sup>A. Johansson, U. Svanberg, and P. E. Hodgson, Ark. Fys. 19, 541 (1961); E. Hagberg, A. Ingermarsson, and B. Sundqvist, Phys. Scr. 3, 245 (1971).
- <sup>13</sup>G. Bruge, CEN Saclay Internal Report No. DPh-N/ME/78-1.
- <sup>14</sup>G. S. Blanpied *et al.*, Phys. Rev. Lett. 39, 1447 (1977).
- <sup>15</sup>R. Bertini *et al.*, Phys. Lett. 45B, 119 (1973).
- <sup>16</sup>R. Humphreys, Nucl. Phys. A182, 580 (1972).
- <sup>17</sup>R. D. Bent *et al.*, Indiana University Cyclotron Facility (IUCF) Internal Report No. 73-1 (unpublished); IUCF Technical and Scientific Report, 1976, p. 22.
- <sup>18</sup>A. Nadasen, Ph.D. thesis, Indiana University, 1977 (unpublished), available as IUCF Internal Report No. 77-5.
- <sup>19</sup>M. Nakamura *et al.*, RCNP Annual Report, Osaka University, 1977, p. 129.
- <sup>20</sup>C. Rolland *et al.*, Nucl. Phys. 80, 625 (1966); P. Hillman, A. Johansson, and H. Tyren, *ibid.* 4, 648 (1957); A. Willis *et al.*, J. Phys. 30, 13 (1969).
- <sup>21</sup>P. Schwandt *et al.*, IUCF Scientific and Technical Report, 1979, p. 47.
- <sup>22</sup>P. Schwandt, IUCF Internal Report No. 77-8 (unpublished).
- <sup>23</sup>F. D. Becchetti, Jr. and G. W. Greenlees, Phys. Rev. 182, 1190 (1969).
- <sup>24</sup>P. Schwandt, Bull. Am. Phys. Soc. 24, 824 (1979); IUCF Scientific and Technical Report, 1979, p. 47.
- <sup>25</sup>The mechanisms for  $\sigma^+$  dominance are different at low and high energies. At low energy,  $\sigma^+ > \sigma^-$  at large angles because the predominately real nuclear potential is more attractive in the spin state  $\vec{\sigma} \cdot \hat{n} = +1$ , while at high energy  $\sigma^+ > \sigma^-$  because of strong absorption [cf., E. Fermi, Nuovo Cimento II, Suppl. 1, 84 (1955)].
- <sup>26</sup>P. Schwandt *et al.*, Bull. Am. Phys. Soc. 24, 614 (1979); IUCF Scientific and Technical Report, 1978, p. 24.
- <sup>27</sup>A. Bohr and B. R. Mottelson, *Nuclear Structure* (Benjamin, New York, 1969), Vol. 1, p. 239.
- <sup>28</sup>S. G. Cooper and P. E. Hodgson, J. Phys. G 6, L21 (1980).
- <sup>29</sup>F. A. Brieva and J. R. Rook, Nucl. Phys. A291, 299 (1977); 317 (1977); A297, 206 (1978); A307, 493 (1978).
- <sup>30</sup>J.-P. Jeukenne, A. Lejeune, and C. Mahaux, Phys. Rev. C 16, 80 (1977).
- <sup>31</sup>A. K. Kerman, H. McManus, and R. M. Thaler, Ann. Phys. (N.Y.) 8, 551 (1959).
- <sup>32</sup>P. Schwandt, F. Petrovich, and A. Picklesimer, IUCF Scientific and Technical Report, 1978, p. 27.
- <sup>33</sup>W. G. Love *et al.*, Phys. Lett. 73B, 277 (1978).
- <sup>34</sup>R. F. Carlson *et al.*, Phys. Rev. C 12, 1167 (1975); J. J. H. Menet, E. E. Gross, J. J. Malanify, and A. Zucker, *ibid.* C 4, 1114 (1971); P. Kirby and W. T. Link, Can. J. Phys. 44, 1847 (1966); A. Johansson, U. Svanberg, and O. Sundberg, Ark. Fys. 19, 527 (1961).
- <sup>35</sup>H. A. Bethe, Phys. Rev. 57, 1125 (1940); M. M. Shapiro, *ibid.* 90, 171 (1953).
- <sup>36</sup>P. U. Renberg *et al.*, Nucl. Phys. A183, 81 (1972).
- <sup>37</sup>K. Kikuchi and M. Kawai, *Nuclear Matter and Nuclear Reactions* (North-Holland, Amsterdam, 1968), p. 33.
- <sup>38</sup>P. Schwaller *et al.*, Nucl. Phys. A316, 317 (1979).
- <sup>39</sup>W. Grein, Nucl. Phys. B131, 225 (1977).
- <sup>40</sup>H. V. von Geramb and G. Palla, Synopsis of Theoretical Nuclear Physics (University of Hamburg Institute for Experimental Physics report, 1978/79), p. 138.
- <sup>41</sup>M. Jaminon, C. Mahaux, and P. Rochus, Phys. Rev. Lett. 43, 1097 (1979); L. G. Arnold and B. C. Clark, Phys. Lett. 84B, 46 (1979).
- <sup>42</sup>B. C. Clark and L. G. Arnold, Bull. Am. Phys. Soc. 25, 520 (1980).